

2

CLIMATOLOGICAL STUDY FOR UNDERSTANDING THE AEROSOL RADIATIVE EFFECTS AT SOUTHWEST ATLANTIC COAST OF EUROPE

4 **Sorribas, M.¹, Andrews, E.², Ogren, J.A.³, del Águila, A.^{1,a}, Fraile, R.⁴, Sheridan, P.³ and Yela,
6 M.¹**

8 ¹Atmospheric Sounding Station – El Arenosillo, Atmospheric Research and Instrumentation Branch,
INTA, Mazagón, Huelva, 21130, Spain

10 ²University of Colorado, CIRES, Boulder, CO 80309, USA

³Earth System Research Laboratory, NOAA, Boulder, CO, 80305, USA

12 ⁴Department of Applied Physics, IMARENAB, University of León, SE-24071, León, Spain

14 ^aformerly at: Atmospheric Sounding Station – El Arenosillo Atmospheric Research and Instrumentation
Branch, INTA, Mazagón, Huelva, 21130, Spain

16 Corresponding author: Mar Sorribas (sorribasm@inta.es)

18 ABSTRACT

In order to describe the means, variability and trends of the aerosol radiative effects on the southwest
20 Atlantic coast of Europe, 11 years of aerosol light scattering (σ_{sp}) and 4 years of aerosol light absorption
(σ_{ap}) are analyzed. A 2006-2016 trend analysis of σ_{sp} for $D < 10\mu\text{m}$ indicates statistically significant trends
22 for March, May-June and September-November, with a decreasing trend ranging from -1.5 to -2.8 Mm^{-1}
/year. In the 2009-2016 period, the decreasing trend is only observed for the months of June and
24 September. For scattering Ångström exponent (SAE) there is an increasing trend during June with a rate
of 0.059/year and a decreasing trend during October with -0.060/year. The trends observed may be
26 caused by a reduction of Saharan dust aerosol or a drop in particle loading in anthropogenic influenced
air masses. The relationship between SAE and absorption Ångström exponent is used to assess the
28 aerosol typing. Based on this typing, the sub-micron particles are dominated by black carbon, mixed
black and brown carbon or marine with anthropogenic influences, while the super-micrometer particles
30 are desert dust and sea spray aerosol. The mean and standard deviation of the dry aerosol direct
radiative effect at the top of the atmosphere (DRE_{TOA}) are $-4.7 \pm 4.2 \text{ W m}^{-2}$. DRE_{TOA} for marine aerosol
32 shows all observations more negative than -4 W m^{-2} and for anthropogenic aerosol type, DRE_{TOA} ranges
from -5.0 to -13.0 W m^{-2} . DRE_{TOA} of regional marine aerosol ranges from -3 to -7 W m^{-2} , as it consists of a
34 mixture of sea salt and anthropogenic aerosol. The variability in DRE_{TOA} is mainly dependent on AOD,
36 given that variations in backscatter fraction and the single scattering albedo tend to counteract each
other in the radiative forcing efficiency equation. The results shown here may help in interpretation of
satellite retrieval products and provide context for model evaluation.

38

40 Highlights:

42

- Trend analyses detect aerosol changes from 2006 to 2016 in southwestern Europe
- It is proposed that the trends may be related to specific climatic changes
- There is a cooling aerosol direct radiative effect (DRE_{TOA} is $-4.7 \pm 4.2 \text{ W m}^{-2}$)
- DRE_{TOA} depends mainly on AOD as b and SSA counteract each other in forcing equation

46 **Keywords:** atmosphere, aerosol optical properties, aerosol radiative effects, trend analysis, climate
48 change

50

1. INTRODUCTION

Atmospheric aerosols are an essential climate forcing agent and play a critical role in global climate change (IPCC, 2014). The effect of aerosols on Earth's radiative budget is determined by their optical properties, including scattering and absorption. Changes in these properties will thus alter the radiative forcing of aerosols. The aerosol climate effects have been enhanced due to anthropogenic aerosol particles (mainly sulfate and carbonaceous substances), which have modified the atmospheric composition substantially (Boucher et al., 2013). The ability of particles to interact with solar radiation is dependent upon particle size and composition, both closely related to variation in sources. The sources of particles within the sub- ($D < 1\mu\text{m}$) and super-micrometer ($1 \mu\text{m} < D < 10\mu\text{m}$) size fractions differ, with sub-micrometer particles commonly deriving from combustion emissions and secondary formation, while super-micrometer fraction generally come from mechanical action (e.g. wind-blown dust or ocean wave breaking) (Seinfeld and Pandis, 1998). Because particle composition varies between sub- and super-micrometer size fractions, the effectiveness with which particles absorb and scatter solar radiation in these two size ranges is also different.

Long-term trends are of interest because they help us understand the global and regional cycling of aerosols with both natural and anthropogenic origin. Aerosol loading and its properties are measured by both ground-based instruments and satellite-borne sensors. There are numerous studies about global or regional aerosol trends, using satellite observations (e.g. Mao et al., 2014) or column integrated data (e.g. Li et al., 2014; Mateos et al., 2014; Cachorro et al., 2016), while only limited studies employ near-surface in-situ aerosol optical measurements (e.g., Collaud et al., 2013; Sherman et al., 2015; Sheridan et al., 2016; Pandolfi et al., 2017). Near the surface, the monitoring of regional or global variation in aerosol properties due to different mixes of sources and atmospheric processing is often addressed by using data from networks of observational sites.

In order to characterize the means, variability and trends of the aerosol properties, the National Institute for Aerospace Technology (INTA) established a long-term monitoring program in southwestern Spain in 2002. This rural-coastal background area was considered of interest because it is frequently affected by African dust episodes with large mineral dust particle loads (Toledano et al., 2007a; Sorribas et al., 2015a; 2017). In this context, scattering measurements started in 2006 and they continue through the present. From 2012, the collaboration between INTA and the National Oceanic & Atmospheric Administration (NOAA) in USA has enabled a strengthening of the aerosol studies, through the deployment of a Continuous Light Absorption photometer (CLAP) (Ogren et al., 2017) and the software for data acquisition and processing, editing and archiving of scattering and absorption data (Andrews et al., 2018).

Analysis of the near-surface in-situ particle light scattering and absorption made with $D < 1 \mu\text{m}$ and $D < 10 \mu\text{m}$ size cuts (effectively PM1 and PM10) are reported in this study. The relationships between various intensive optical parameters (those which are independent of particle number) are also analyzed. As complementary data, column-integrated aerosol optical depth are brought in to determine the direct aerosol radiative forcing. This work provides a picture of the atmospheric conditions on the southwest Atlantic coast of Europe in terms of aerosol properties. The major goals of this study are to answer the following questions:

1. What are typical values, temporal variability and trends of aerosol optical properties?
2. How do the aerosol optical properties over the Southwest Europe compare to other places?
3. What is the size- and composition- dependent variability of aerosol optical properties?
4. How does the radiative forcing depend on aerosol type and size fraction?

The answers to these questions may help to put in context remote sensing retrieval products so they can better be used to minimize uncertainties in satellite retrievals comparison of aerosol properties (e.g.

104 Kahn et al., 2017). These results can be also used in model evaluation studies, because models must
106 correctly parameterize aerosol properties in order to properly simulate the forcing by aerosols (e.g.
108 Cuevas et al., 2015; Péré et al., 2018). The complementarity between the data presented here and those
from satellite and models provides valuable information into the optical properties of the atmosphere
and the radiative effect of aerosol.

110 **2. METHODOLOGY**

111 **2.1. Site description**

112 The sampling site is located at El Arenosillo (ARN) observatory (37.18N, 6.78W, 40 m a.s.l.) in the
114 southwest of the Iberian Peninsula. The site is located in a protected rural environment (the Doñana
116 National Park), 0.7 km from the coast of the Atlantic Ocean, in the mouth of the Guadalquivir valley, and
118 close to the Mediterranean Sea and North African coast. Previous research at El Arenosillo has shown
120 that the site can be impacted by dust, biomass burning, marine aerosol and anthropogenic emissions
122 (from industry/population centers in the Guadalquivir valley), depending on time of year and air flow
patterns. More information regarding the atmospheric aerosol characterization in this area can be found
e.g.: in Toledano et al. (2007a; 2007b) where a description of integrated-column data is shown;
Córdoba-Jabonero et al. (2011) with a characterization of the medium-range transport episode of desert
dust by lidar-sun-photometric-nephelometric techniques and Sorribas et al. (2011; 2015a; 2015b; 2017)
describing the in-situ aerosol in terms of sub- and super-micrometer size ranges as well as optical
properties (scattering, backscattering and absorption).

124 **2.2. Measurements and instrumentation**

126 **2.2.1. Aerosol sampling system description**

128 The sampling system inlet used during January 2006-September 2009 period was partly described in
130 Sorribas et al. (2015c). It consisted of an external vertical stainless steel pipe (9.8 cm inner diameter and
550 cm length). The bottom part of the outer pipe was positioned nearly concentrically around two
132 inner pipes with a 1 cm and 2.5 cm inner diameter, which served as particle size and particle optical
property sampling lines, respectively. The aerosol sample was transported into the laboratory without
sharp bends in the tubing to minimize particle losses. The flow rate and the Reynolds number in-pipe for
134 the optical properties were 30 lpm and 1655, respectively. The sampling system efficiency calculated
according to Willeke and Baron (1993), ranged from 99% for 100 nm particles to 50% for 12 μm particle
diameter.

136 From October 2009 to the present, a new aerosol sampling system inlet design was used. The inlet
138 system for optical properties measurements consists of a vertical stainless steel pipe (2.3 cm inner
140 diameter and 300 cm length), which directs the aerosol into the instruments at a flowrate of 30 lpm and
a Reynolds number of 1799. A PM10 inlet head (Thermo Scientific™) is used as a first step to size
142 segregation. The 30 lpm flowrate is almost double the 16.7 lpm design flow, making the cutpoint about
7 μm particle aerodynamic diameter. The contribution to the aerosol optical properties between 7-10
144 microns is considered negligible at ARN. A second step to size segregation is a switched impactor
146 system, also using 30 lpm flowrate. It consists of a multiple orifice impactor with a cutpoint of 1 μm
particle diameter, and a valve that alternately is opened and closed every 5 min to measure sub1-
148 micron and sub10-micron size fractions. The super-micron size fraction ($1 \mu\text{m} < D < 10 \mu\text{m}$) is estimated
from the difference between the sub1- and sub10-microns size fractions. Due to malfunctions of the
software and hardware, which caused the switching valve to be stuck in open position, several longer
gaps of aerosol optical properties in the sub1-micrometer size fraction exist in the dataset.

150 After July 2012, a dilution system is used to reduce the relative humidity of the aerosol sample. Dry
152 particle-free air is produced by an air compressor dryer system and is introduced to a sample-mixing
154 tube. This tube is a commercial unit fabricated by Mott Corporation (Farmington, CT, USA, part number
76101100-100). To obtain an adequate mixing of the dilution and sample air, a vertical tube of length 1
m is used. In this work, the relative humidity threshold for valid measurements is RH < 60%.

156 The inlet configurations are consistent with the sampling inlet recommendations of the WMO Global
158 Atmospheric Watch program. See <http://www.wmo-gaw-wcc-aerosol-physics.org/files/WCCAP-recommendation-for-aerosol-inlets-and-sampling-tubes.pdf>.

160 **2.2.2. Integrating nephelometer**

162 Aerosol particle scattering (σ_{sp}) and hemispheric backscatter (σ_{bsp}) coefficients were measured using a
164 three wavelength integrating nephelometer (TSI, Model 3563), operating at 450, 550 and 700 nm
166 (Anderson et al., 1996). A weekly maintenance and calibration check of the nephelometer is carried out
168 using CO₂ and filtered air. Data were corrected for truncation errors according to Anderson and Ogren
170 (1998), using the tabulated factors for total and submicron scatter as a linear function of scattering
172 Ångström exponent. The continuous monitoring of scattering and back-scattering data at El Arenosillo
174 Observatory started in January 2006 and data through December 2016 are analyzed in this study. Due to
176 malfunctions of the instrument, there is a 7 month gap in the dataset from May to November 2008.

178 The uncertainties in total scattering and hemispheric backscatter coefficients are estimated following
180 Sherman et al. (2015). The major uncertainties in σ_{sp} and σ_{bsp} measured by the TSI 3563 nephelometer
182 are (1) uncertainty in the nephelometer calibration using filtered air and CO₂ gases ($\Delta\sigma_{sp,cal}$), (2)
184 nephelometer calibration variability ($\Delta\sigma_{sp,var}$), (3) uncertainty in the correction for nephelometer angular
186 non-idealities ($\Delta\sigma_{sp,trunc}$), (4) uncertainty in correcting σ_{sp} and σ_{bsp} to standard temperature and pressure
(STP) conditions ($\Delta\sigma_{sp,tsp}$), (5) uncertainties in correcting σ_{sp} and σ_{bsp} to 40% relative humidity during
humid periods ($\Delta\sigma_{sp,RH}$). $\Delta\sigma_{sp,cal}$, $\Delta\sigma_{sp,trunc}$ ($D<10\mu m$ and $D<1\mu m$) and $\Delta\sigma_{sp,tsp}$ are obtained from prior
reported values, as is shown in Table 1. $\Delta\sigma_{sp,var}$, $\Delta\sigma_{sp,RH}$ are estimated for the nephelometer running at
ARN observatory as described below.

188 *Estimation of $\Delta\sigma_{sp,var}$* – Based on 328 nephelometer span check errors over eight years (2009-2016) at
190 ARN, the variability in the nephelometer calibrations is estimated. During (2006-2008) period, no
information about the span check error is available, although it is expected to be consistent with those
observed during (2009-2016) period, which are shown in Table 1. $\Delta\sigma_{sp,var}$ values are shown in Table 1,
192 and range from 2.3% to 3.9%. Sheridan et al. (2002) and Sherman et al. (2015) reported similar values in
previous studies.

Unit:%	σ_{sp} 450 nm	σ_{sp} 550 nm	σ_{sp} 700 nm	σ_{bsp} 450 nm	σ_{bsp} 550 nm	σ_{bsp} 700 nm	Reference
$\Delta\sigma_{sp,cal}$	7.0	7.0	7.0	7.0	7.0	7.0	Anderson et al. 1998
$\Delta\sigma_{sp,var}$	2.3	2.9	3.9	2.5	2.8	3.8	This work
$\Delta\sigma_{sp,trunc}$ ($D<10\mu m$)	5.0	4.6	4.2	3.8	3.8	4.0	Anderson and Ogren (1998)
$\Delta\sigma_{sp,trunc}$ ($D<1\mu m$)	1.0	0.7	0.4	0.9	0.9	1.0	Anderson and Ogren (1998)
$\Delta\sigma_{sp,tsp}$	0.4	0.4	0.4	0.4	0.4	0.4	Sheridan et al. (2002)
$\Delta\sigma_{sp,RH}$ (Period 1)	<5	<5	<5	<5	<5	<5	
$\Delta\sigma_{sp,RH}$ (Period 2)	<15	<15	<15	<15	<15	<15	This work

188 **Table 1.** Uncertainties expressed as a percentage in total scattering and hemispheric backscatter
190 coefficients at 450, 550, 700 nm. In the particular case of $\Delta\sigma_{sp,RH}$, two periods are considered. Period 1:
all dataset except Period 2. Period 2: from June to November in 2006 and 2009 years.

192 *Estimation of $\Delta\sigma_{sp,RH}$* – Figure 1S shows an analysis of the relative humidity variability in the aerosol
194 sampled in terms of the monthly (2006-2016) dataset. During much of the analyzed time period, the
196 aerosol sampling system was not conditioned to achieve a relative humidity lower than 40%, as the
198 World Meteorological Organization recommends (WMO, 2016). To ensure appropriate temporal
coverage in this multiyear study, a relative humidity threshold value of 60% was applied. This may have
shifted the scattering coefficients towards higher values by < 5% (Sorribas et al., 2015a). During 2006
and 2009 years (in particular from June to November which is called Period 2 in Table 1), there was a
very large number of hourly means of scattering coefficients monitored with RH higher than 60%. For

200 that time period, a new restriction on data was applied (RH<70%), increasing the uncertainties in
201 aerosol optical properties due to RH effects up to 15% (more information in Section 2.3).

202 **2.2.3. Light absorption photometer**

204 The Continuous Light Absorption Photometer (CLAP) is a NOAA-designed and built instrument used to
205 measure aerosol absorption (σ_{ap}) at 467, 528 and 652 nm by means of a filter-based technique (Ogren et
206 al., 2017). It uses a single 47-mm filter with 10 filter spots: two alternate as reference spots, while the
207 other eight are sampled consecutively. Switching to the next sample spot is automated and occurs when
208 the light transmission through the filter falls below 0.7. Because the CLAP was developed to be
209 functionally comparable to the Particle/Soot Absorption Photometer (PSAP, Radiance Research), the
210 Bond et al. (1999) and Ogren (2010) corrections for aerosol scattering and transmission through the
211 filter are applied. The continuous monitoring of absorption data at El Arenosillo Observatory started in
212 July 2012. Due to malfunctions of the instrument, the CLAP data set for our study stops in September
213 2016.

214 Ogren et al. (2017) shows the CLAP with the main design features, noise characteristics and uncertainty
215 description. The detection limits of the attenuation coefficient for use in excluding noise results was
216 estimated from the standard deviation of the CLAP when measuring filtered air. It was parametrized as
217 $0.10 \text{ Mm}^{-1} * (\Delta t / 100 \text{ s})^n$, with $n = -1$ for $5 \text{ s} < \Delta t < 100 \text{ s}$ and $n = -0.5$ for $100 \text{ s} < \Delta t \leq 24 \text{ h}$. Since the
218 nephelometer+CLAP system at ARN was used with a switched impactor, the hourly/daily averages
219 correspond to 1800/43200 seconds, respectively, for each size cut. For those averaging times, the noise
220 of the CLAP is 0.024 and 0.0048 Mm^{-1} , respectively. It is recommended to exclude the CLAP data when
221 the attenuation coefficient is less than twice these values (Ogren, personal communication), e.g., 0.048
222 and 0.0096 Mm^{-1} for hourly/daily means, although values in this range are not observed at ARN. Ogren
223 et al. (2017) also shows that values of both the single scattering albedo and attenuation coefficient are
224 needed to derive the uncertainty of the absorption coefficient. An analysis of the CLAP uncertainties at
225 several NOAA and collaborators sampling stations concluded that the lowest uncertainties are seen for
226 stations with higher absorption and lower single scattering albedo, such as observed at ARN. The
227 percent uncertainty in absorption at ARN is between 22-33%, assuming 1800 seconds averaging time
228 and a single scattering albedo within the 0.84-0.94 range.

229 **2.2.4. Cimel Sun-Photometer**

230 In order to estimate the direct aerosol radiative forcing, data from a CIMEL Sun-Sky Photometer
231 collocated with the in-situ measurements has been used. The CIMEL Sun-Sky photometer measures
232 direct solar radiation at eight nominal wavelengths: 340, 380, 440, 500, 675, 870, 940 and 1020 nm. The
233 full-width of the filters at half maximum is 10 nm for all wavelengths, except those at 380 nm with 4 nm
234 and at 340 nm with 2 nm. The calibration of the direct component was performed by transference from
235 an instrument with a recent calibration made using the Langley plot derived from measurements at a
236 high mountain site. The irradiance calibration uncertainty for the instruments is 1-2%, depending on the
237 channel (Holben et al., 1998). In the present work, aerosol optical depth (AOD) was obtained using the
238 ESR.PACK code. The ESR.PACK code is based on the SKYRAD.PACK algorithm used in the international
239 network of SKYNET (Takamura and Nakajima, 2004) but it has been modified for application to CIMEL
240 sky-sun photometers. The AOT retrieved by ESR.PACK is comparable to the retrieval of the most
241 extensive photometric network, the NASA Aerosol Robotic Network (AERONET), with mean bias
242 deviation values between -0.0030 and + 0.0041 (0.012 in the case of AOD at 340 nm) (Estellés et al.,
243 2012). In the present work, AOD was calculated for the period between July 2012 and May 2014, to
244 overlap with nephelometer and CLAP measurements. Unfortunately, a malfunction of the sun-
245 photometer resulted in missing AOD data from April 2013 to February 2014.

246 **2.3. Processing of data step by step**

247 To prepare the data for analysis the followed steps have been carried out:

252 *Step 1* - the aerosol optical properties were sampled at 1-s resolution and collected at 1-min resolution.
254 The data were quality-checked and edited using ESRL/GMD software (Andrews et al., 2018) to remove
256 spikes caused by electronic glitches, background level changes, malfunction of the impactor switching
module for selecting the particle size cut, span-check time period, filter changes, etc. From this reviewed
data set the hourly means were computed.

258 *Step 2* – The hourly aerosol properties with RH higher than 60% during the entire dataset, except from
260 June to November in 2006 and 2009 years, (e.g. Period 2) were removed. During Period 2 higher values
of RH were observed (see Figure 1S) and the relative humidity threshold value was moved to 70%.

262 *Step 3* – A mean scattering enhancement factor $f(RH)$ is used to correct the nephelometer data
264 monitored with RH in the 60-70% range, as Figure 2S shows. It was estimated on the basis of chemical
266 aerosol composition, as was previously shown in Sorribas et al. (2015a) during a particle density
268 estimation. A value of $f(RH)$ was assumed for each chemical constituent: *Marine* $f(RH=85\%) = 2.2$ (Fierz-
270 Schmidhauser et al., 2010b), *Desert* $f(RH = 85\%) = 1.3$ (Zieger et al., 2013), *Organic+Inorganic* (sub-
micrometer) $f(RH=85\%) = 2.2$ and *Organic+Inorganic* (super-micrometer) $f(RH=85\%) = 2.4$ (Titos et al.,
2014a). The variability of $f(RH)$ for each aerosol species within the super-micrometer size range, is
higher than for the lower size fraction. Average $f(RH=70\%)$ within the sub- and super-micrometer size
ranges is quite similar and is estimated to be 1.15.

272 To demonstrate the magnitude of the error during the $f(RH)$ estimation, a short analysis is performed,
274 assuming the extreme $f(RH=70\%)$ values observed at ARN within the super-micrometer size fraction.
276 Desert dust aerosol is found to be less hygroscopic than marine aerosol particles (Figure 2S) with
278 $f(RH=70\%)$ values of 1.08 and 1.27, respectively. Thus, scattering coefficient may be shifted higher by up
to 27%, in the presence of marine aerosol during Period 2. If the average $f(RH=70\%)$ is considered, the
shift to higher scattering is likely less than 15% (see Table 1) during Period 2.

280 *Step 4* – Finally, hourly aerosol intensive properties are calculated in order to characterize the nature of
282 the aerosol. The intensive properties calculated here are the scattering Ångström Exponent (SAE),
284 absorption Ångström Exponent (AAE), the fraction of backscattered light (b), single scattering albedo
286 (SSA), asymmetry factor (g) and radiative forcing efficiency (RFE). Most of these have been extensively
288 defined in previous references (e.g., Sheridan and Ogren, 1999; Sorribas et al., 2015a). SAE and AAE
290 were calculated for the 450/550 nm wavelength pairs while other values are reported for the 550 nm
wavelength. The asymmetry factor is derived through the parametrization in Andrews et al. (2006). The
292 constant parameters used in RFE calculation are the solar constant of 1370 W m^{-2} , the atmospheric
294 transmission of 0.76, the surface reflectance of 0.15 for coniferous forest (Oke, 1987), the fractional
296 cloud amount and day length values depend on the analysis explained below, while the aerosol single
298 scattering albedo and aerosol upscatter fraction used in the RFE calculation come from the
measurements and depend on time. The upscatter fraction estimation is carried out using the
300 parametrization in Sheridan and Ogren, 1999 and Andrews et al. (2006). The fractional cloud amount
and day length are considered as constant with values 0.6 and 0.5, respectively, in the annual and
302 seasonal climatologies and the estimation of optical properties for each aerosol type (Sections 3.2
through 3.5). These assumptions were intended to minimize the influence of these environmental
304 properties on the variability of the aerosol properties with the aim to study the nature of the aerosol.
306 For the direct radiative effect estimation (Section 3.6), the fractional day length is calculated at the
308 latitude of the sampling site as function of the day of the year and the fractional cloud amount is
310 estimated by using the percent of photometric measurements with respect to the total, following
312 implementation of the cloud screening control.

314 Calculations of intensive parameters often rely on ratios of measured parameters; at low loading, the
316 calculated values are less reliable due to instrument noise and constraints on measured parameters are
318 often used to minimize noise in the intensive parameters. For example, Schmeisser et al. (2017) only

304 calculated aerosol intensive parameters for cases where the $\sigma_{sp} > 1 \text{ Mm}^{-1}$ and $\sigma_{ap} > 0.5 \text{ Mm}^{-1}$ at 550 nm
306 wavelength. However, the threshold for CLAP data of $\sigma_{ap} > 0.5 \text{ Mm}^{-1}$ is too restrictive when pure marine
308 aerosol is measured. This type of aerosol is characterized by low absorption but high scattering
310 coefficients. From a manual inspection of the ARN data set, when $\sigma_{ap} < 0.5 \text{ Mm}^{-1}$ and single scattering
312 albedo is higher than 0.992, some intensive aerosol properties (e.g. AAE) exhibit unrealistic values. But,
314 for SSA lower than 0.992, the intensive properties correctly characterize the aerosol. Therefore, we have
316 decided to include in our analysis the intensive properties when $\sigma_{ap} < 0.5 \text{ Mm}^{-1}$ if SSA was lower than
318 0.992.

320 *Step 5* - Hourly time resolution data were averaged to daily time resolution if at least 63% of the hourly
322 measurements (15 hours) of the daily time period were available.

324 Following these processing steps, an analysis of annual trends, annual and seasonal climatology, an
326 assessment of aerosol typing and a study of direct aerosol radiative effect was carried out.

328 **3. RESULTS AND DISCUSSION**

329 **3.1. ANNUAL TRENDS**

330 Trend analysis has been used to determine if the optical properties over time are going up, down or
332 staying the same. In the literature, several procedures have been used to estimate rates of change of
334 atmospheric constituents. If the data conform to a normal distribution, a regression analysis provides
336 information about the trend but if the frequency distribution of the data set is normal or log-normal, the
338 Mann-Kendall (MK) test can be applied. The MK test does not require the data to be normally
340 distributed and evaluates whether y values tend to increase or decrease over time through what is
342 essentially a nonparametric form of monotonic trend regression analysis. Moreover, the MK test has
344 low sensitivity to inhomogeneous time series with abrupt breaks such as data losses, and the statistical
346 significance of the trend can be determined. To determine the magnitude of the trend, Sen's method
348 was used (Gilbert, 1987).

350 A trend analysis for σ_{sp} and SAE has been carried out. At ARN, extensive properties (e.g. σ_{sp}) are
352 described well by a log-normal distribution while intensive properties (e.g. SAE) have a normal
354 distribution (Sorribas et al., 2015a), therefore, the MK test is used for both properties. The MK test was
356 applied to analyse the yearly (Figure 1) and monthly trends (i.e., trends for each individual month for the
358 entire data set). Monthly means were calculated only if 60% of the days of each month are available
360 (more than 18 days/month). The analysis covers an 11 year data set but, due to malfunctions or sample
362 relative humidity higher than 60% (more information in Section 2.3), there are some years where data
364 for some months does not meet this criteria. A complete monthly time series would have 11 values (one
366 for each year) but some months had fewer (as low as 5). The least complete time series occurred in the
368 summer months. When the number of values in the time series is less than ten, the MK test was carried
370 out using the so-called *S statistics* given in Gilbert (1987), while if it was higher than ten, the normal
372 approximation is used.

374 In the trend analysis presented here, the only analysed data were those corresponding to scattering
376 properties with $D < 10 \mu\text{m}$, because the temporal coverage for $D < 1 \mu\text{m}$ scattering properties was quite
378 sparse during some years (e.g., 2010 and 2016). The downward trend for $\sigma_{sp}(D < 10 \mu\text{m})$ in Figure 1a is
380 more pronounced over the period 2006-2009, so the annual tendency has been analysed for two
382 different time periods (2006-2016) and (2009-2016) (see Table 2). For absorption no analysis is shown,
384 as the data set is quite short; Figure 1b suggests the annual means of absorption exhibit no clear trend.
386 A trend analysis on aerosol absorption will be done in the future as more data become available.

388 Table 2 lists the results for the trend analysis and provides the Sen's parameters. Negative/positive MK
390 Statistic (*S*) indicates a downward/upward trend and the Kendall's Tau (comparable to correlation
392 coefficient for a linear regression) shows the goodness of the relationship. For $\sigma_{sp}(D < 10 \mu\text{m})$ and the

(2006-2016) period, the test indicates statistically significant trends for March, May-June and September-November periods with a level of confidence $p < 0.1$. The decreasing trend ranges from -1.5 to -2.8 $\text{Mm}^{-1}/\text{year}$, with the highest values during the September-October period. This decrease in atmospheric scattering is also reflected in the significant decreasing trend for (2006-2016) annual averages, with a calculated decreasing trend of -2.2 $\text{Mm}^{-1}/\text{year}$. For the (2009-2016) period, the decreasing trend is less obvious and although it is identified, it is only statistically significant ($p < 0.1$) for June and September months (see Table 2). When the decreasing trends (in absolute terms) for (2006-2016) and (2009-2016) periods are compared, it is noteworthy that the decreasing rate in June and September are similar for the first period and higher for the second period. Previous work also shows a decreasing trend in the south of Europe, but trend values are not given (Pandolfi et al., 2017).

366

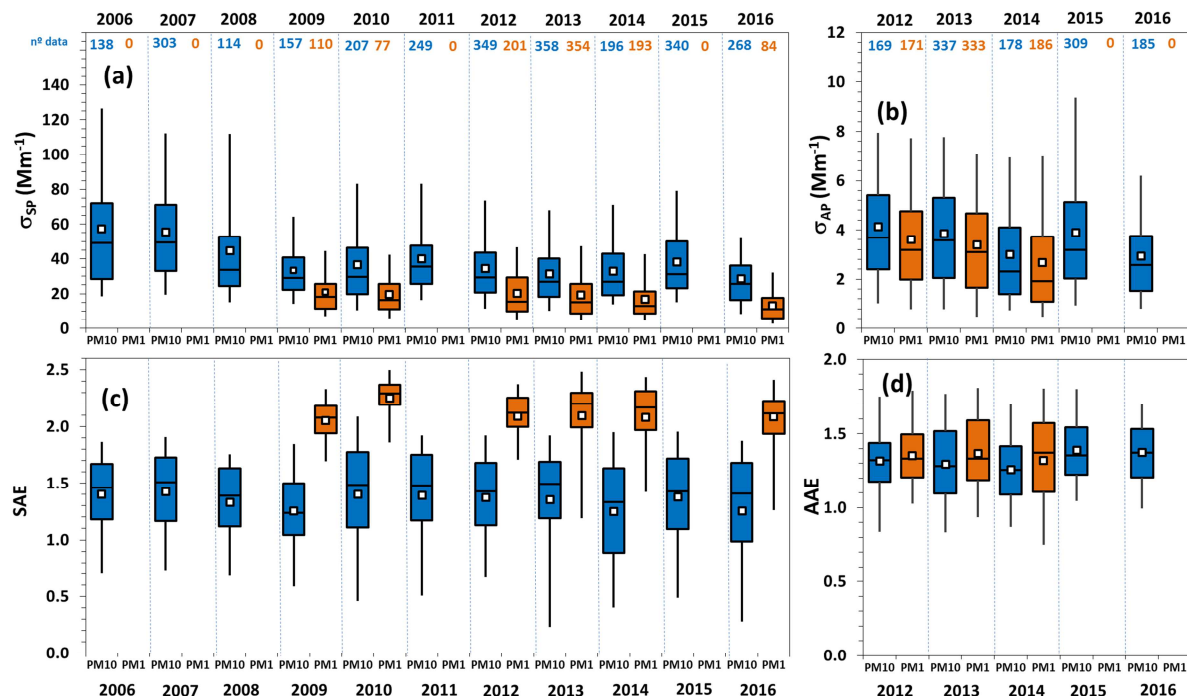


Figure 1. Box-whisker time series of annual average (based on daily averages) of aerosol (a) scattering at 550 nm, (b) absorption at 550 nm, (c) scattering Ångström exponent at (450/550 nm) and (d) absorption Ångström exponent at (450/550 nm). The horizontal line in each box is the median (50th percentile), edges of each box are the 25th and 75th percentiles, and the whiskers indicate the 5th and 95th percentiles. The white square in each box is the mean value. Blue boxes are for particles with $D < 10 \mu\text{m}$ and orange boxes for $D < 1 \mu\text{m}$. The number of days used in each box-whisker marker is shown at the top of figures (a) and (b).

374

For SAE, the behaviour was quite similar during (2006-2016) and (2009-2016) periods. There were two monthly trends (June and October) with p values lower than 0.1. During both periods, the increasing trend during June was 0.059/year. During October, the opposite behaviour was observed with a decreasing trend -0.060/year (for 2006-2016) to -0.072/year (for 2009-2016).

380 Scattering coefficient depends on the particle number concentration and size and, therefore, the tendency observed for σ_{sp} may be explained by a decrease in the particle number concentration within 382 fine and coarse size fractions, as anthropogenic and mineral dust, respectively. Because SAE is an 384 indicator of the contribution of fine and coarse mode aerosols, it is also potentially useful to infer 386 aerosol composition. Therefore, these trends in SAE and σ_{sp} suggest a change in not only the monthly aerosol loading but also in monthly composition. For the June trend, the σ_{sp} reduction and SAE increase might be mainly linked to a reduction in natural sources such as coarse mode mineral dust. For the

October trend, the σ_{sp} and SAE reduction might be due to a drop mainly in fine-mode anthropogenic emissions, leaving an aerosol dominated by natural sources such as sea salt.

Previous statistical analyses have been carried out in Europe to detect and estimate the trend in aerosol properties. Li et al. (2014) focus on aerosol optical depth (AOD), column extinction Ångström Exponent (EAE) and some inversion products including absorption aerosol optical depth (AAOD), column single-scattering albedo and the column absorption Ångström Exponent derived from the Aerosol Robotic Network (AERONET) products. Data from El Arenosillo are used in their study but the trends they found were not statistically significant. However, Li et al. (2014) suggested that, in general, the southern Iberian Peninsula experienced a uniform decrease in AOD and EAE, suggesting changes in particle loading and fine/coarse mode fraction. This is consistent with the observed reduction in the Saharan desert dust outbreaks in the north-central area of the Iberian Peninsula (Cachorro et al., 2016). The number of desert dust events between 2003 and 2014 have decreased by 0.67 episodes per year, corresponding to a decrease in the total number of dusty days of 2.7 days per year. Cachorro et al. (2016) have also analysed the inter-annual variability of the desert dust contributions to PM_{10} , $PM_{2.5}$ and $PM_{2.5-10}$ concentrations, showing a decreasing trend in particle concentration for the three size fractions.

		2006-2016 period							2009-2016 period						
		n	S	Tau	Q	B	Sign.	Trend	n	S	Tau	Q	B	Sign.	Trend
σ_{sp}	Jan	7	-3	-0.14	--	--	--	⊗	6	3	0.20	--	--	--	⊗
	Feb	9	-14	-0.39	-4.0	61.6	^	↓	7	-1	-0.05	--	--	--	⊗
	Mar	8	-20	-0.71	-1.5	46.3	*	↓	6	-9	-0.60	-1.7	47.7	^	↓
	Apr	9	-4	-0.11	--	--	--	⊗	8	10	-0.36	--	--	--	⊗
	May	9	-18	-0.50	-1.9	43.9	x	↓	8	-10	-0.36	--	--	--	⊗
	Jun	8	-20	-0.71	-1.4	42.3	*	↓	7	-13	-0.62	-1.4	42.3	x	↓
	Jul	7	-5	-0.24	--	--	--	⊗	5	4	0.40	--	--	--	⊗
	Aug	6	-3	-0.20	--	--	--	⊗	5	-2	-0.20	--	--	--	⊗
	Sep	5	-10	-1.00	-2.0	51.5	*	↓	4	-6	-1.00	-3.6	62.1	x	↓
	Oct	8	-16	-0.57	-2.6	48.3	x	↓	6	-5	-0.33	--	--	--	⊗
	Nov	8	-14	-0.50	-2.8	41.4	x	↓	6	-5	-0.33	--	--	--	⊗
	Dec	8	-10	-0.36	--	--	--	⊗	7	-5	-0.24	--	--	--	⊗
SAE	Annual	11	--	-2.65 (Test Z)	-2.2	50.2	**	↓	8	-8	-0.29	-0.7	38.716	--	⊗
	Jan	7	-9	-0.43	-0.063	1.81	^	↓	6	-9	-0.60	-0.127	2.45	^	↓
	Feb	9	-16	-0.44	-0.073	1.76	^	↓	7	-11	-0.52	-0.121	2.16	^	↓
	Mar	8	4	0.14	--	--	--	⊗	6	1	0.07	--	--	--	⊗
	Apr	9	-2	-0.06	--	--	--	⊗	8	6	0.29	--	--	--	⊗
	May	9	-12	-0.33	-0.025	1.46	^	↓	8	-10	-0.36	--	--	--	⊗
	Jun	8	20	-0.71	0.059	0.92	*	↑	7	13	0.62	0.059	0.88	x	↑
	Jul	7	3	0.14	--	--	--	⊗	5	4	0.40	--	--	--	⊗
	Aug	6	-1	-0.07	--	--	--	⊗	5	0	0.00	--	--	--	⊗
	Sep	5	2	0.20	--	--	--	⊗	4	-2	-0.33	--	--	--	⊗
	Oct	8	-16	-0.57	-0.060	1.73	x	↓	6	-13	-0.87	-0.072	1.82	*	↓
	Nov	8	-8	-0.29	--	--	--	⊗	6	1	0.07	--	--	--	⊗
	Dec	8	0	0.00	--	--	--	⊗	7	7	0.33	0.046	1.12	^	↑
	Annual	11	--	-1.56 (Test Z)	--	--	--	⊗	8	-8	-0.29	--	--	--	⊗

Table 2. Annual and seasonal Mann-Kendall trend analysis for the scattering coefficient and SAE, corresponding to (2006-2016) and (2009-2016) periods. In the table header, n represents the number of points, S is the Mann-Kendall Statistic, Tau represents the Kendall's Tau, Q in $Mm^{-1}/year$ and B in Mm^{-1} are the slope and the intercept of the existing trend estimated by Sen's method. The significance (Sign.) and interpretation of the trend are also indicated. Levels of significance are (**) $p<0.01$, (*) $p<0.05$, (x) $p<0.1$ and (^) $p<0.2$. Interpretation of the trend is (↑) increasing, (↓) decreasing, and (⊗) no trend.

410

In this context, the σ_{sp} and SAE trends presented in this study can be explained assuming a combination of one or more of the following causes: (1) reduction in the frequency of Saharan desert dust air masses arriving in the south of Spain, (2) a decrease in particle loading in desert dust air masses and/or (3) a drop in particle loading in anthropogenically influenced air masses.

416 **3.2. ANNUAL CLIMATOLOGY**

418 The annual mean values of aerosol optical properties $\sigma_{sp}(D<1\mu m)$ and $\sigma_{sp}(D<10\mu m)$ calculated from
420 hourly averages (*daily averages*), along with their standard deviations are $19\pm17\text{ Mm}^{-1}$ ($18\pm13\text{ Mm}^{-1}$)
422 and $37\pm31\text{ Mm}^{-1}$ ($38\pm25\text{ Mm}^{-1}$), respectively. Previous studies at ARN covering shorter periods show
424 quite similar values, for example Sorribas et al. (2015a) with five months of data (May-September) reported mean scattering coefficients of $21\pm15\text{ Mm}^{-1}$ and $34\pm19\text{ Mm}^{-1}$ for $D<1\mu m$ and $D<10\mu m$ size ranges respectively. A large peak in the scattering record during February 2016 has been attributed to a strong and anomalous desert dust episode (Sorribas et al., 2017), but this does not appear to have significantly affected the 2016 annual statistics for σ_{sp} or SAE.

426 Typical values of the hourly (*daily averages*) of $\sigma_{ap}(D<1\mu m)$ and $\sigma_{ap}(D<10\mu m)$ are $3.3\pm2.7\text{ Mm}^{-1}$ ($3.2\pm2.2\text{ Mm}^{-1}$) and $4.0\pm2.9\text{ Mm}^{-1}$ ($3.6\pm2.4\text{ Mm}^{-1}$), respectively, showing that the absorbing particles are mainly within the sub1-micron size range. The highest amount of σ_{ap} observed at ARN occurred during the desert dust episode in February 2016 with σ_{ap} reaching 23 Mm^{-1} ($D<10\mu m$ size fraction). Single scattering albedo (SSA) was $0.85\pm0.07\text{ Mm}^{-1}$ ($0.85\pm0.05\text{ Mm}^{-1}$) and $0.89\pm0.05\text{ Mm}^{-1}$ ($0.90\pm0.04\text{ Mm}^{-1}$) for sub1-micron and sub10-micron size fraction, respectively, corresponding to darker aerosol within the sub1-micron fraction. Fifty percent of the hourly observations of SSA($D<10\mu m$) were lower than 0.9, while 18% were lower than 0.85. For SSA($D<1\mu m$), 74%, 46%, 21% and 7% were lower than 0.9, 0.85, 0.80 and 0.75, respectively. While anomalously high σ_{ap} values were observed during the 2016 [dust advection episode](#), the SSA values during that event were consistent with the long-term observations. 436 Clean marine sites exhibit higher SSA values than [observed at](#) ARN due to predominantly white sea salt aerosol (Andrews et al., 2018). Lower SSA denotes periods/episodes where the contribution of 438 absorption increased, due primarily to anthropogenic (continental air masses) and dust aerosol.

440 Comparison of ARN's mean annual values of scattering and absorption coefficients with other 442 anthropogenically influenced coastal sites around [the](#) world, shows that they are higher than those found in Cape Cod (Massachusetts, north eastern United States) with mean $\sigma_{sp}(D<10\mu m)$ of $22\pm15\text{ Mm}^{-1}$ and mean $\sigma_{ap}(D<10\mu m)$ of $1.1\pm0.9\text{ Mm}^{-1}$, respectively (Titos et al., 2014b). Scattering values at 444 ARN are similar to those measured at the Sable Island (WSA) site, which is an eastern Canada marine site occasionally impacted by continental outflow and lower than the scattering at highly polluted 446 marine sites such as GSN and AMY sites in Asia (Andrews et al., 2018).

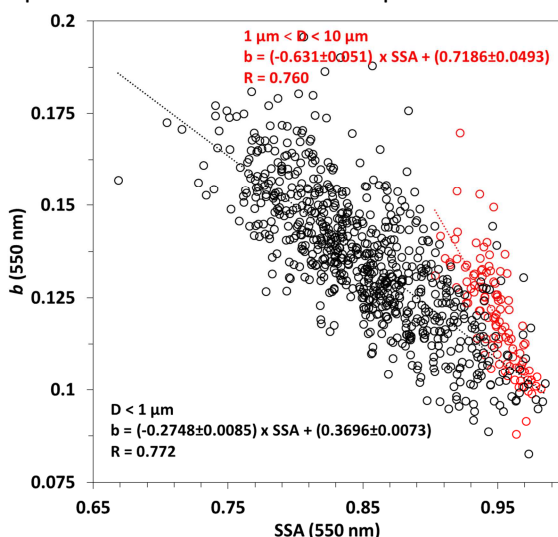
448 At El Arenosillo, mean values of SAE($D<10\mu m$) were 1.3 ± 0.6 (1.4 ± 0.4) and for SAE($D<1\mu m$) were 2.1 ± 0.4 (2.1 ± 0.3), which is quite high relative to those found in the literature for clean marine aerosol (e.g. 450 Carrico et al., 1998; Andrews et al., 2018). These SAE values are evidence of the mixed aerosol 452 contribution at El Arenosillo: the high values of SAE indicate a more pronounced contribution of smaller 454 particles to scattering. The hourly (daily) value of AAE was $1.34\pm0.33\text{ Mm}^{-1}$ ($1.33\pm0.27\text{ Mm}^{-1}$) and 456 1.37 ± 0.46 ($1.35\pm0.29\text{ Mm}^{-1}$) for ($D<1\mu m$) and ($D<10\mu m$) size fractions, respectively. AAE, can be used to 458 characterize some of the aerosol composition: AAE lower than 1 is indicative of carbonaceous aerosol as 460 elemental carbon, while biomass smoke and desert dust can reach values in excess of 1.5 (Cappa et al., 2016). The average values of AAE observed at ARN and their standard deviation are representative of 462 mixed aerosols, as well as aged and processed aerosols in the air masses arriving at ARN. The AAE values 464 also highlight that El Arenosillo is on the Atlantic coast and occasionally samples marine air: for marine 466 aerosol the spectral dependence of aerosol absorption is low, resulting in lower values for AAE.

468 The backscatter fraction (b) is an important climate parameter as particle radiative effects depend, in 470 part, on the extent to which incoming solar radiation is reflected back to space versus absorbed within 472 the Earth system. It mainly depends on particle size and chemical composition (Horvath et al., 2015). 474 Hourly (*daily*) averages of b within ($D<1\mu m$) and ($D<10\mu m$) are $0.14\pm0.04\text{ Mm}^{-1}$ ($0.14\pm0.02\text{ Mm}^{-1}$) and 476 0.12 ± 0.03 ($0.13\pm0.02\text{ Mm}^{-1}$). These ranges of observed values are comparable to measurements made

466 at other locations on the Iberian Peninsula (e.g., 0.14 in Granada City (Lyamani et al., 2010) and 0.13 in
 468 Evora, Portugal (Pereira et al., 2011)). SAE and b are both related to aerosol mean size, but are sensitive
 470 to different parts of the size distribution. SAE is more sensitive to the largest diameters of the
 472 accumulation mode particles ($D > 0.7 \mu\text{m}$), while b is sensitive to the smaller diameters ($D < 0.4 \mu\text{m}$)
 (Collaud Coen et al., 2007). Our study finds that SAE and b have a low correlation with $R^2 = 0.22$ and 0.30
 for micron and sub1-micron size fractions, respectively. This is likely a result of a broad and/or multi-
 modal size distribution impacted by various sources across the year (Sorribas et al., 2011).

474 The angular distribution of light scattered by aerosols, namely, the aerosol phase function, is
 476 represented by the asymmetry factor (g). g is higher for larger particles such as marine aerosol,
 478 compared to g for continental or urban aerosols. The value for g can range from -1 (pure backscatter)
 480 to +1 (pure forward scatter), but negative values of g occur only for small metallic particles and are not
 482 relevant for the ambient atmosphere. Therefore, only values of the asymmetry parameter g between 0
 (symmetric scatter) and +1 (pure forward scatter) need to be considered (Moosmüller and Ogren, 2017).
 At ARN, the mean g values within ($D < 1 \mu\text{m}$) and ($D < 10 \mu\text{m}$) are 0.58 ± 0.06 (0.58 ± 0.05) and 0.58 ± 0.19
 (0.60 ± 0.04), respectively. These values are similar to those in Fiebig and Ogren (2006), which shows a
 climatology of g at several locations in the NOAA aerosol monitoring network.

484 Calculation of the aerosol radiative forcing efficiency allows evaluation of the direct radiative effect for
 486 each type of aerosol (e.g., marine, dust, etc). The hourly (daily) mean RFE for ($D < 1 \mu\text{m}$) and ($D < 10 \mu\text{m}$)
 488 are (-19.1 ± 4.3) (-19.2 ± 3.1) $\text{W m}^{-2} \text{ AOD}^{-1}$ and (-22.1 ± 2.8) (-23.3 ± 2.5) $\text{W m}^{-2} \text{ AOD}^{-1}$, respectively. The low
 490 values of standard deviation mean that only a small range in RFE is observed at the site. The relationship
 492 between b and SSA values is one of the reasons for this low variability, as they effectively counteract
 each other in the RFE equation. This correspondence is shown in Figure 2 with a high anti-correlation
 coefficient ($R = 0.76$) for super micron and sub1-micron size fractions. This suggest that the variability in
 direct radiative effect in southwest Europe (estimated using RFE*AOD) is mainly dependent on the
 variability on AOD, i.e., the impact of aerosol on total atmospheric column.



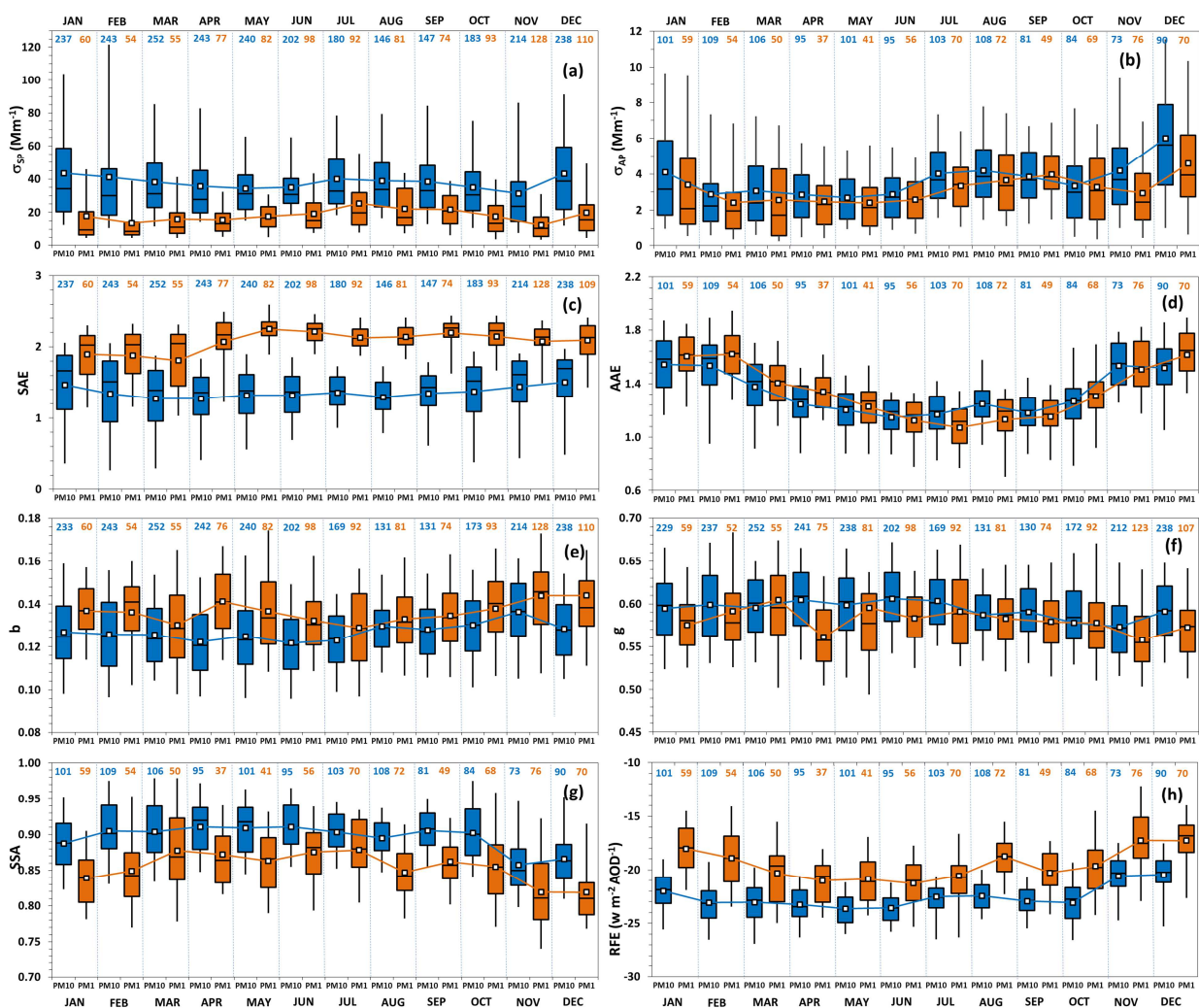
494 **Figure 2.** Relationship between backscatter fraction (b) and single scattering albedo (SSA) at 550nm
 496 within sub- (black points) and super-micrometer (red points) size fractions.

3.3. TEMPORAL CLIMATOLOGY

498 The sampling site is located in a coastal environment and there is a frequently observed local circulation
 500 diurnal wind pattern (the sea-land breeze phenomenon), especially in spring and summer time.
 502 However, none of the optical parameters reported on here showed a clear diurnal pattern. Sorribas et
 al. (2011) analyzed the effect of the sea-land breeze on the particle concentration in terms of sub-
 micrometer size distribution. They found that the highest impact of the sea-land breeze pattern was
 mainly on the ultrafine mode (particle diameter lower than $0.1 \mu\text{m}$), while the effect on concentration

504 for particles with larger diameter was weaker. The optical properties reported on here are most
 506 sensitive to particles with diameter larger than $0.1\text{ }\mu\text{m}$ (Sorribas et al., 2015a) and that likely explains the
 lack of an observed diurnal cycle.

508 Seasonal cycles were analyzed from the daily-averaged data classified according to the measurement
 510 month. A clear seasonal cycle was found in both the scattering and absorption coefficient (Figures 3a
 and 3b) with two maxima occurring. The maximum values of both $\sigma_{\text{sp}}(D<1\mu\text{m})$ and $\sigma_{\text{sp}}(D<10\mu\text{m})$ were
 512 observed at about the same times of the year in December-January and July-August. The minimum of
 514 $\sigma_{\text{sp}}(D<1\mu\text{m})$ occurred in February and November and that of $\sigma_{\text{sp}}(D<10\mu\text{m})$ in May and November. The
 516 high values of scattering during summer are probably related to natural sources such as desert dust (the
 typical dust season in the southern part of Europe is the warm period (Toledano et al., 2007a), and
 518 during winter to medium-range transport of continental air masses (Toledano et al., 2009). The
 monthly-minimum to monthly-maximum range was $12\text{-}25\text{ Mm}^{-1}$ and $31\text{-}43\text{ Mm}^{-1}$ for $\sigma_{\text{sp}}(D<1\mu\text{m})$ and
 $\sigma_{\text{sp}}(D<10\mu\text{m})$, respectively.



520 **Figure 3.** Statistical analysis showing monthly evolution (based on daily averaged data) for (a) scattering,
 522 (b) absorption, (c) scattering Ångström exponent and (d) absorption Ångström exponent, (e)
 524 backscattering fraction, (f) asymmetry factor, (g) single scattering albedo and (h) radiative forcing
 efficiency. Data are reported at 550 nm , except the scattering and absorption Ångström exponent
 values, which are calculated for the $450/550\text{ nm}$ pair. Number of daily means are shown at the top of
 each figure. The horizontal line in each box is the median (50th percentile), edges of each box are the

526 25th and 75th percentiles, and the whiskers indicate the 5th and 95th percentiles. The white square in each
528 box is the mean value. Blue for (D < 10 μm) and orange for (D < 1 μm).

529 The highest values in σ_{ap} were observed in December while lower values occurred in February-June
530 period. The higher values during December may be related to an increase of fuel and wood combustion
531 for domestic heating in cities throughout [Guadalquivir's Valley](#). SSA (Figure 3g) shows lower values of
532 about 0.86 and 0.82 during November-December for sub- and super-micrometer size fractions
533 respectively, when absorption and scattering are the highest, indicating higher contribution for
534 absorption in terms of extinction properties relative to other months. This is also consistent with the
535 seasonal behaviour in the radiative forcing efficiency (RFE) within D<10 μm (Figure 3h), which peaks (in
536 absolute terms) in cold months. The monthly-minimum to monthly-maximum range in absorption was
537 2.4-4.6 Mm^{-1} for $\sigma_{\text{ap}}(\text{D}<1\mu\text{m})$ and 2.7-6.0 Mm^{-1} $\sigma_{\text{ap}}(\text{D}<10\mu\text{m})$.

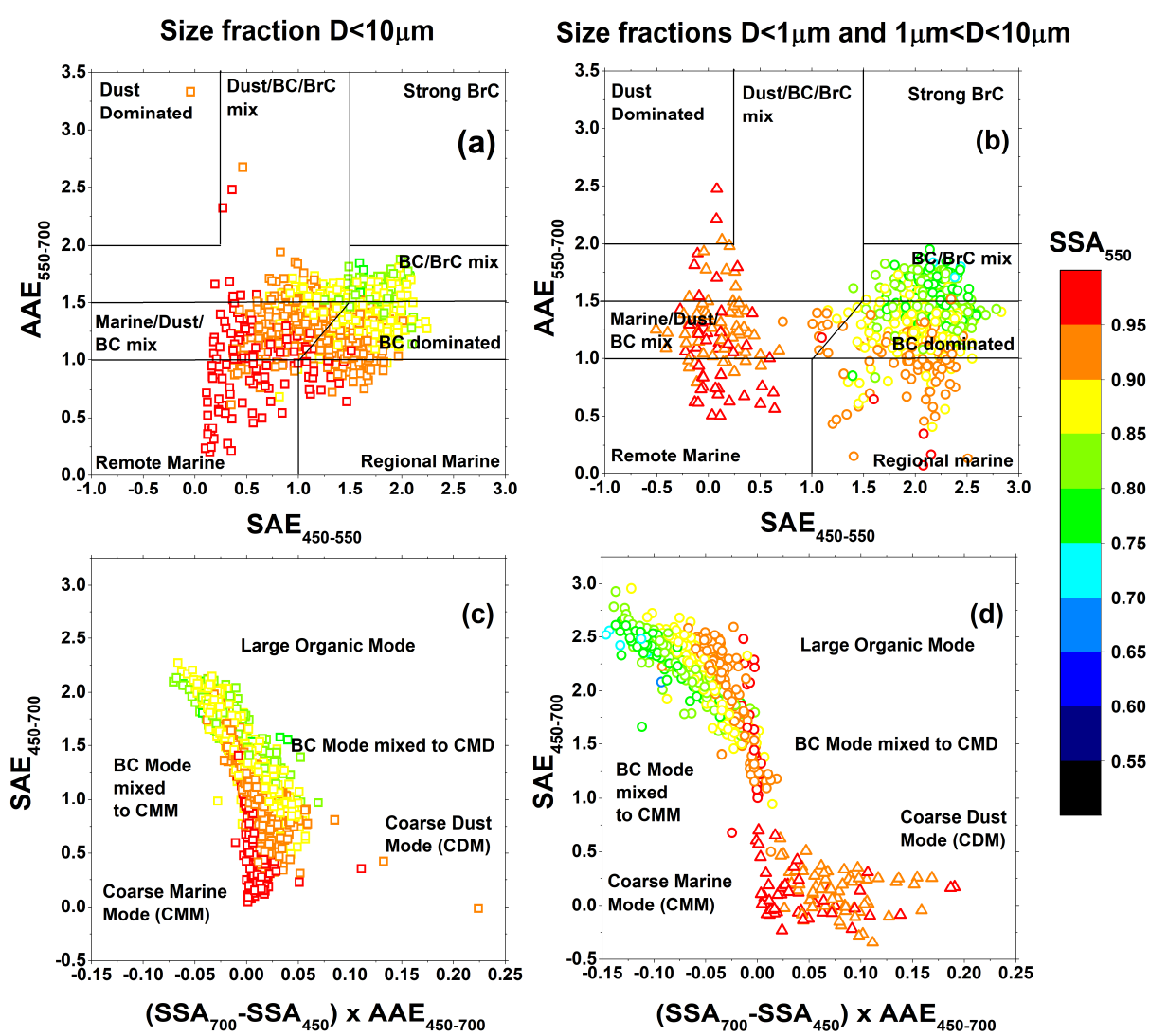
538 There is not a pronounced seasonality in the SAE (D<10 μm) (Figure 3c), probably due to the aerosol
539 being composed of a mix from several aerosol sources. However, the variability in SAE is larger during
540 the cold months, when maritime air masses (sea salt aerosol contribution) at 500 m are more frequent
541 (Toledano et al., 2009), resulting in the larger range of SAE displayed in the box-whisker plots. The
542 seasonal behaviour of SAE (D<1 μm) exhibits lower values during January-March months, probably due
543 to a sea-salt contribution in the sub1-micron range. Seasonal behaviour is more obvious in the AAE data.
544 During warm months, AAE values lower than 1.2 were found, while during cold months AAE was higher
545 than 1.5. This suggests, in combination with the increase of σ_{ap} also observed during cold months, that
546 there is a predominance of wood combustion heating sources impacting the southwest Atlantic coast of
547 Europe.

548 The seasonal cycle of the backscattering fraction, b (Figure 3e), is quite modest, with a weak increase in
549 spring (April) and November. This increase was probably caused by the smaller mean particle sizes of
550 secondary aerosol particles (i.e. new particle formation (NPF)). NPF through homogeneous gas-phase
551 processes, followed by the condensation growth of the freshly nucleated particles to optically active
552 size, occurs commonly in this sampling area with higher frequency in April and November (Sorribas et
553 al., 2015c). The seasonal cycle in b is inversely correlated with that of the asymmetry factor (Figure 3f).

554 **3.4. ASSESSMENT OF AEROSOL TYPING**
555 The relationship between SAE and AAE provides information on aerosol composition and size, and can
556 suggest a particular aerosol type (e.g. Cazorla et al., 2013; Costabile et al., 2013; Cappa et al., 2016;
557 Schmeisser et al., 2017). In our study the relationship among daily averages of SAE, AAE and SSA are
558 presented in Figure 4 to investigate aerosol type at El Arenosillo. The similarities and differences
559 between Cazorla et al. (2013) and Cappa et al. (2016) have been explained in a previous work
560 (Schmeisser et al., 2017). In our work, we use the Cappa et al. (2016) matrix (Figure 4a for D<10 μm size
561 fraction and Figure 4b for D<1 μm and 1 μm <D<10 μm size fractions) since it is based on in situ data,
562 while Cazorla et al. (2013) is based on integrated column data. But a slight variation in the Cappa
563 classification is followed here. The version used here changes: (1) "large particles/ low absorption mix"
564 in the lower left plot space designation to "Remote marine", (2) "Small particle/low absorption mix" to
565 "Regional marine" and (3) "Large particle/ BC mix" to "Marine/Dust/BC mix" as these correspond to
566 data presented here. The aerosol typing has also been qualitatively corroborated using back-trajectories
567 (briefly discussed in Text T1 in supplemental materials). Cappa's matrix is also compared to the chemical
568 paradigm in Costabile et al. (2013) which uses chemical composition data and numerical simulations to
569 validate the proposed classification scheme (Figure 4c for D<10 μm size fraction and Figure 4d for
570 D<1 μm and 1 μm <D<10 μm size fractions).

571 Figure 4a, and following the results in Schmeisser et al. (2017), illustrates that the expected dominant
572 aerosol sources at ARN are continental polluted (black carbon (BC)-dominated), marine polluted
573 (regional marine) and continental dust/biomass (mixed dust, BC and Brown Carbon (BrC)). BrC is

578 identified as the light absorbing fraction of organic matter emitted from biomass burning. BC at ARN is
 580 related to aged anthropogenic aerosol with large variety in origin and history, including most of the
 582 Iberian Peninsula and/or Europe. BC may also be emitted by flaming and smoldering fires. Regional
 584 marine aerosol is transported over the Mediterranean Sea and Atlantic Ocean, but is also likely
 586 influenced by anthropogenic aerosol (e.g. BC). The Cappa classification scheme also enables
 588 identification of events with dominant aerosol types of natural origin (e.g. marine and desert dust).
 Remote marine aerosol is related to pure marine aerosol originated from the Atlantic open ocean (e.g.
 sea salt), which has not been transported over land. Dust dominated aerosol arrives at the sampling site
 directly from the Saharan desert. It is necessary to emphasize, that due to the constraints on measured
 σ_{ap} (Section 2.2), some pure marine aerosol events may be excluded from the analyzed data.



592 **Figure 4. (Upper)** $AAE_{550-700}$ vs. $SAE_{450-550}$ daily means (2012-2016 period) with points color-coded by
 594 SSA_{550} . The plot is overlaid with the aerosol classification matrix from Cappa et al. (2016) for (a) $D < 10 \mu m$
 596 size fraction (open squares) and for (b) $D < 1 \mu m$ (open circles) and $1 \mu m < D < 10 \mu m$ (open triangles) size
 598 fractions. **(Lower)** Relation observed between SAE and $(SSA_{700}-SSA_{450}) \times AAE_{450-700}$ with points color-coded
 600 by SSA_{550} as Costabile et al. (2013) proposed for illustrating the “paradigm” to classify aerosol
 populations for (c) $D < 10 \mu m$ size fraction (open squares) and for (d) $D < 1 \mu m$ (open circles) and $1 \mu m < D < 10 \mu m$ (open triangles) size fractions.

The SSA variability observed in Figure 4a, occurs because SSA depends on both particle size and composition. SSA values > 0.95 are related to large particles with relatively low absorption and is dominated by marine and dust aerosol, but also mixed with black carbon. The interval $0.90 < \text{SSA} < 0.95$ is related to a wide range of particle sizes and likely represents mixtures of dust/marine and BC. For $0.85 < \text{SSA} < 0.90$ the characterized particles have shifted to smaller diameters and higher BC and BrC contribution than would be seen for pure dust aerosol. Finally, when $\text{SSA} < 0.85$ the atmospheric aerosol mostly contain a mixture of particles with BC and BrC contributions. Figure 4a demonstrates that SSA in conjunction with spectral information about scattering and absorption can be used as tracer of aerosol typing.

The assessment of aerosol typing shown previously is also compared to the aerosol classification paradigm proposed by Costabile et al. (2013) in Figures 4c and 4d. These figures show $d\text{SSA} \times \text{AAE}$ on the x-axis and SAE on the y-axis for different size fractions. Our observations are consistent with the results of the Costabile's paradigm, showing a similar classification of the aerosol population.

If a segregation by particle size (as parameterized by SAE) is carried out on optical properties (Figure 4b), it needs to be stressed that the number of daily averages is considerably lower than actually available for the sub10-micrometer size fraction. This is because constraints are needed on absorption coefficients when the intensive properties are calculated (see Section 2.2). In this particular case, the unrealistic values for AAE occur when $\sigma_{ap} < 0.5 \text{ Mm}^{-1}$, regardless of SSA. This could possibly be explained by measurement limitations. The absorption at 700 nm is going to be the lowest absorption observed for the three CLAP wavelengths so the calculations will be the noisiest. Details of the segregation by particle size and the correspondence between the points found in Figures 4a and 4b can be found below.

The first difference between the two size fractions is that, while SSA for super-micrometer particles is mainly higher than 0.95, SSA for sub1-micron particles ranges from 0.55 to 0.95. In Figure 4b, the sub1-micrometer data fall primarily in the space encompassed by $\text{SAE} > 1$ and $1 < \text{AAE} < 2$. These particles are classified as BC dominated and mixed BC/BrC, as values of AAE higher than 1.5 have been related to absorbing organic carbon (Cazorla et al., 2013). The data points falling in Cappa's BC dominated and BC/BrC categories within sub10-micron (Figure 4a) and sub1-micron (Figure 4b) represent the same days. Figure 4b also shows some data points corresponding to small particles with low absorption ($\text{SSA} > 0.9$) and values of $\text{AAE} < 1$. These data fall within the regional marine category. The data points falling in Cappa's regional marine category within sub10-micron (Figure 4a) and sub1-micron (Figure 4b) represent the same days. In Sorribas et al. (2015a) the chemical composition of the sub1-micrometer aerosols at ARN was shown to consist primarily of secondary inorganic compounds (SIA: SO_4 , NO_3 and NH_4) and organic matter. SIA compounds can be a result of secondary formation from their gaseous precursors as (SO_2 , NO_x and NH_3 , respectively). SO_4 can be also related to primary aerosol emission from seawater.

The super-micrometer particles are classified in three groups in Figure 4b. The first group indicates a remote marine aerosol category with $\text{SAE} < 0.25$ and $\text{AAE} < 1$. These daily means correspond to the super-micrometer size fraction of the daily means shown in Figure 4a within the regional marine category. The data points representing remote marine aerosol identified in Figure 4a do not appear on Figure 4b because the super-micrometer fraction are comprised of primarily white aerosol ([those cooling the atmosphere](#)) and do not meet the constraints we have imposed on absorption coefficients (i.e., $\sigma_{ap} > 0.5$). The second group shows a wide range of $\text{AAE} > 1$ and $\text{SAE} < 1$, suggesting a mixture of sea salt and dust in varying amounts. Cappa's matrix suggests BC or BrC may also contribute to this second group. The third group is the dust contribution, which is clearly identified with $\text{SAE} < 0.25$ and $\text{AAE} > 2$ because dust is able to absorb infrared radiation.

652 The dust contribution at ARN requires further discussion. Because of the geographical location of ARN
654 on the south-west **coastal** border of Spain, the aerosol properties of desert dust layers tend to be a mix
656 between dust and marine particles in varying amounts. During the 109 days with simultaneous
658 scattering and absorption monitoring in both size cuts such that the super-micrometer optical
660 properties could be determined, only 3 days indicated a predominance of dust (Figure 4b) at the
662 surface. These same days showed sub-micron optical properties classified as 'BC dominated' near to the
664 boundaries for the BC/BrC mix in Cappa's matrix. A previous analysis relating the submicron particle size
666 distribution to the different air mass types at ARN (Sorribas et al., 2011) showed similar volume size
668 distributions for desert dust and continental aerosol particles. These size distributions were unimodal
670 (single peaked) with modal diameter within (300-350) nm. Given that the contribution of mineral
672 aerosol within the submicron size fraction is low, this suggests that the increase in sub-micrometer
674 particle size fraction related to air masses coming from African continent may be related to African
676 biomass burning (Roberts et al., 2009) and North African industrial pollutants (Rodríguez et al., 2011). In
678 addition, Sorribas et al. (2015) also shows that typical desert dust episodes over ARN take place under a
680 mixture of Mediterranean and North African flows. Therefore, additional Mediterranean particle
682 sources may also contribute to the submicron size fraction during desert dust episodes.

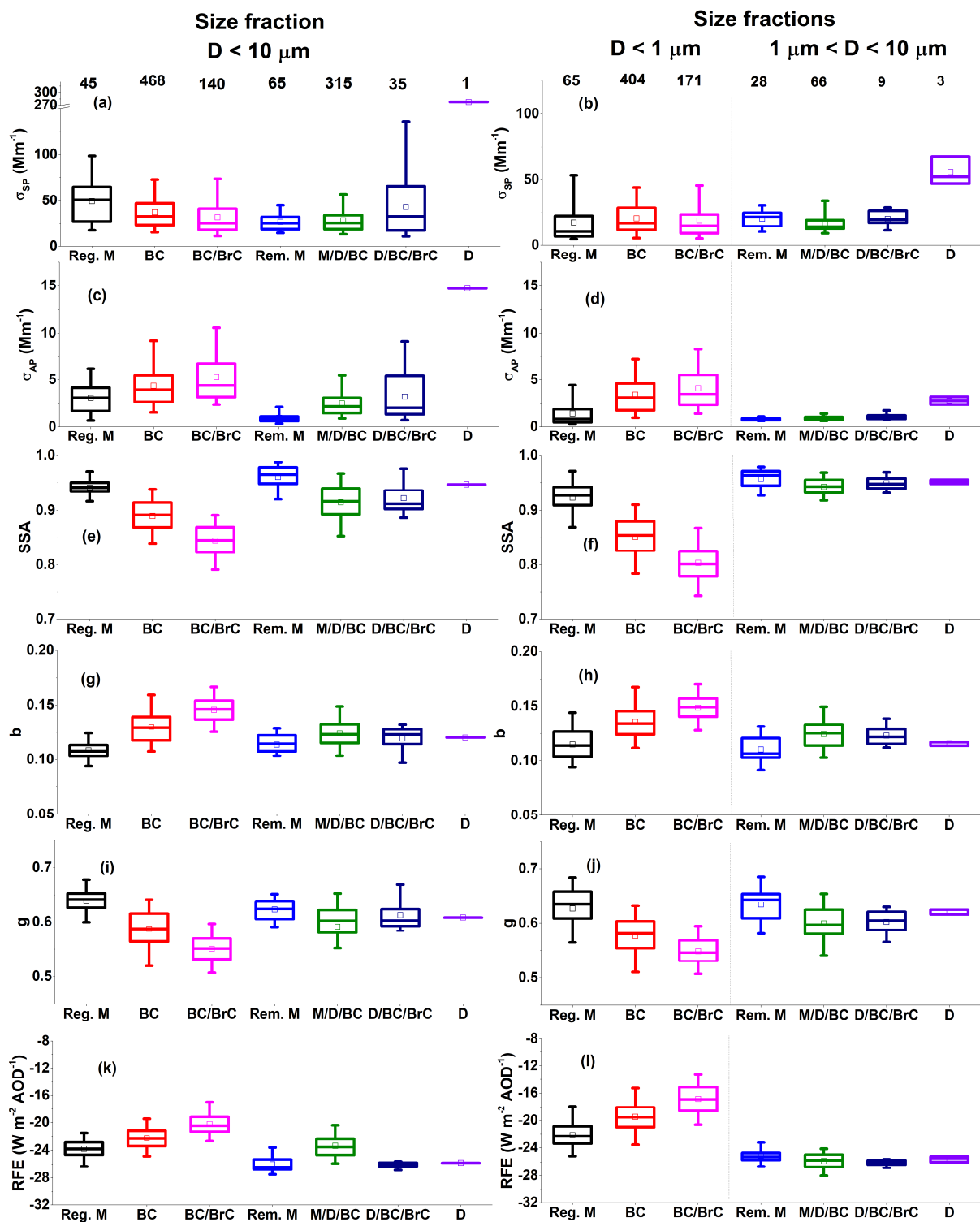
3.5. OPTICAL AND PHYSICAL PROPERTIES FOR EACH AEROSOL TYPE

670 Following the segregation of aerosol typing in Figure 4, the main aerosol properties are studied in terms
672 of the particle size fraction and the aerosol type. The aerosol types are identified for each daily data
674 point using the relationship between SAE and AAE and the boundaries of different aerosol types in
676 Figure 4a and 4b. This enables characterization of the aerosol properties for each type. Figure 5
678 summarizes this statistical analysis, within $D < 10 \mu\text{m}$ (left) and $D < 1 \mu\text{m}$ and $1 \mu\text{m} < D < 10 \mu\text{m}$ (right). In
680 general, the aerosol property statistics for each aerosol type are quite similar for each size fraction.

682 The dust type for $D < 10 \mu\text{m}$ (Figure 5a) shows σ_{sp} higher than 270 Mm^{-1} . This high value corresponds to
684 levels observed during 22th February 2016, when a dust transport phenomenon arrived at southwest
686 Atlantic coast of Europe. This episode was exceptional because of its unusual intensity during the cold
688 season and it was an example of an extreme atmospheric event occurring in a hotspot, the Saharan
690 desert, and its impact two thousand km away (Sorribas et al., 2017). Unfortunately, the scattering values
692 for dust segregated by size (Figure 5b) are unavailable during this event due to a malfunction of the
694 switched impactor system. Consequently, σ_{sp} values for dust in Figures 5a and 5b, represent different
696 time periods. All aerosol types in Figure 5b, except dust, exhibit σ_{sp} with daily mean values from 17 to 20
 Mm^{-1} , while dust values are significantly higher ($56 \pm 11 \text{ Mm}^{-1}$) despite not encompassing the February
2016 event. Another observation is that there is a slight increase in variability for sub-micrometer size
fraction relative to the super-micrometer size fraction, as 25th and 75th percentiles shown in Figure 5b.
This is likely because air masses dominated by natural aerosol (dust/marine) within the super-
micrometer size fraction are less variable than those within the sub1-micron fraction.

698 Absorbing particles are primarily contained within the submicron size fraction (Figures 5d and 5f). σ_{ap} is
700 higher for the brown and black carbon mixture (BC/BrC category) with a daily mean of 4.0 Mm^{-1} , while
702 the lowest absorption values are observed for the regional marine group (1.4 Mm^{-1}). The low absorption
values for the regional marine group are consistent with the characterization of sea salt aerosols as non-
light-absorbing particles. Black and brown carbon absorption coefficients on the southwest Atlantic
coast of Europe are similar to those found in other European continental sites (Zanatta et al., 2016).

704 The SSA values for the $D < 1 \mu\text{m}$ size cut are lower than the $D < 10 \mu\text{m}$ SSA values. In contrast, the SSA
706 values for the $1 \mu\text{m} < D < 10 \mu\text{m}$ size cut tend to be higher than the $D < 10 \mu\text{m}$ SSA values. This reflects both
708 that absorbing aerosol is primarily in the sub-micrometer size range and that natural aerosol (e.g., dust
710 and salt) are more likely to be coarse, primarily scattering aerosol.



704 **Figure 5.** Statistics of optical properties for each aerosol type within $D < 10 \mu\text{m}$ (left) and $D < 1 \mu\text{m}$ and $1 \mu\text{m} < D < 10 \mu\text{m}$ (right) size ranges, calculated using the limits of AAE&SAE relationship shown in Figures 4a and 4b. (a and b) Scattering, (c and d) absorption coefficients, (e and f) single scattering albedo (g and h) back-scattering fraction, (i and j) asymmetry factor and (k and l) radiative forcing efficiency (RFE) are shown. The horizontal line in each box is the median (50th percentile), edges of each box are the 25th and 75th percentiles, and the whiskers indicate the 5th and 95th percentiles. Reg. M is regional marine. Rem. M is remote marine. M/D/BC are Marine/Dust/Black Carbon mix contribution. D/BC/BrC are Dust/Black Carbon/Brown Carbon mix contribution. Number of days for each aerosol type is indicated at the top of Figures 5a and 5b.

The backscatter fraction decreases with larger particles since forward scattering increases with particle diameter (e.g. Collaud Coen et al., 2007). Figure 5h suggests that the BC and BC/BrC types (b values ranging from 0.14 to 0.15) are dominated by lower end of the accumulation mode aerosol. In contrast, the regional marine aerosol type exhibits the lowest b value of any of ARN's aerosol types with 0.12 ± 0.02 . Two factors may be related to the low b values for the regional marine group: (1) b is lower for sharp-edged aerosol than for spherical aerosol of the same geometric diameter (Doherty et al., 2005), e.g., regional marine is related to marine aerosol (see Section 3.4) and therefore suggests that sea-salt is more irregular than carbonaceous aerosol or (2) differences in the size distribution of the sub1-micron size fraction for regional marine and carbonaceous aerosol compounds (Collaud Coen et al., 2007), e.g., regional marine compound has higher mean diameter than carbonaceous aerosol. In our case, one issue in opposition to argument the (1) is that the sea salt aerosols are hygroscopic and pick up water at low relative humidity, so they may not be irregular at the relative humidity values at which the measurements are made. The b values for other aerosol types fall between the BC, BC/BrC and regional marine aerosol, again likely reflecting differences in size distribution.

All aerosol compounds except BC and BC/BrC have scattering asymmetry parameter, g , with daily mean values from 0.60 to 0.63 Mm^{-1} (Figure 5j). BC and BC/BrC components show lower mean daily g with values of 0.58 ± 0.03 and 0.55 ± 0.03 , respectively. This is consistent with BC and BC/BrC being associated with smaller anthropogenic particles.

Submicron aerosol components show high radiative forcing efficiency (Figure 5l), RFE, especially those with carbonaceous aerosol in the BC and BC/BrC categories, with mean values of $-17 W m^{-2} AOD^{-1}$. Aerosol types corresponding to larger particles (e.g. dust and marine influenced aerosol types) exhibit lower RFE with values around $-24 W m^{-2} AOD^{-1}$.

3.6. DIRECT AEROSOL RADIATIVE EFFECT

The direct aerosol radiative effect (DRE) of aerosols is the instantaneous radiative impact of atmospheric particles on the Earth's energy balance (Heald et al., 2014). It is sometimes confused with the direct radiative forcing, which is the change in DRE from pre-industrial to present-day. The aerosol direct radiative effect at the top of the atmosphere (DRE_{TOA}) has been estimated for the clear-sky direct solar radiation observational data over ARN using the aerosol optical depth (AOD) observed at 500 nm by a Cimel sun-photometer and the radiative forcing efficiency (RFE) calculated at 550 nm from nephelometer and CLAP measurements. The AOD values were adjusted to 550 nm using Ångström interpolation of the AOD at 500 and 676 nm. DRE_{TOA} was calculated using $DRE_{TOA} = RFE * AOD$. This approach to calculating DRE_{TOA} has several constraints to take into consideration: (1) the different temporal coverage of RFE and AOD, (2) the variability of the environmental properties as fractional cloud amount in the REF equation (see Section 2.3), (3) the potential for different aerosol layers aloft, (4) the dependence between AOD and fractional cloud amount and (5) the variability of ambient relative humidity (RH) at the surface and aloft. These points are discussed further below, and points (4) and (5) are currently under study. It is important to underline that the following results are just approximations, because of the limitation of applying the RFE equation to a particular time and place.

(1) A caveat associated with aerosol DRE_{TOA} estimation using these experimental datasets is the different temporal coverage of each measurement: the AOD is measured during daylight hours and clear-sky direct solar radiation, while RFE is measured with a 1-min time resolution 24 hours/day. In the present work, the uncertainty due to this different temporal coverage has been removed by computing and using the 1-h average nephelometer only for those times during when the Cimel data were retrievable.

(2) The fractional cloud amount, (A_c), is estimated using the percent of sun-photometric measurements with respect to the total, (n), following implementation of the cloud screening algorithm. The cloud screening algorithm eliminates the data affected by clouds. A_c is assumed to be 0, 0.5 or 1 when n is

>75%, within the range [25-75]% and <25%, respectively. This is a simplistic attempt to account for
766 actual A_c and more effort will be carried out in the future with the aim to addressing the deviations in
DRE incurred by the restricted use of three intervals for A_c value.

768 (3) The next consideration for DRE_{TOA} estimation is related to the vertical structure of the atmosphere,
770 which might be an important factor affecting the relationship between integrated column and surface
772 in-situ measurements. In the particular case of the southern Atlantic coast of Europe, the variability in
774 direct radiative effect (estimated using RFE*AOD) is mainly dependent on AOD, as was previously shown
776 in Section 3.2, due to the small range in RFE observed by the relationship between backscattering
778 fraction and the single scattering albedo values. This finding leads to our assumption that the surface
RFE can, in most cases, represent the RFE throughout the column. When DRE_{TOA} was calculated for
specific aerosol types this was further addressed by utilizing the criteria that the aerosol type identified
from the surface measurements was required to match the aerosol type identified for the AOD
measurements (i.e., Toledano et al., 2007b) as described below.

780 (4) The potential co-variance between A_c and AOD is not considered here and as noted above is a
subject of further study. Such a relationship could occur if certain air mass types (and their associated
782 AOD) were more likely to be associated with atmospheric dynamics/meteorology (e.g., frontal passages,
Zhang and Reid, 2009) or if effects like humidification and aerosol processing related to clouds impacted
784 the AOD (e.g., Eck et al., 2018).

786 (5) To quantify the direct effect of aerosol particles in the energy budget, it is required to transform the
dry RFE to ambient conditions (Titos et al., 2014a). The importance of the RH effect was shown by
788 Markowicz et al. (2003) where a 25% increase in RH enhanced the RFE by a 10% during the ACE-Asia
experiment. This dependence was also shown during an experimental campaign in Granada (Spain),
790 where a RH increase from dry conditions (<40%) to 85% increased RFE by about 30% (in absolute terms)
(Titos et al., 2014a). Therefore, the results shown in this section are expected to be affected by the
792 vertical profile of relative humidity which is not available for the analysis. Here, we have utilized the
non-ambient RFE from the in-situ measurements along with the ambient AOD from the sunphotometer
794 measurements. A more detailed study of the effects of RH on aerosol forcing at ARN is planned.

796 The hourly mean value obtained for DRE_{TOA} for all data was -4.7 W m^{-2} with standard deviation, $\pm 4.2 \text{ W}$
 m^{-2} and 5th and 95th percentiles of -13.4 W m^{-2} and -0.77 W m^{-2} , respectively. The frequency histogram of
798 DRE_{TOA} in Figure 6a shows a frequency mode centered between -1.0 W m^{-2} and -2.0 W m^{-2} bins. Positive
values of DRE_{TOA} were not observed.

800 Additionally, DRE_{TOA} estimates based on the single component aerosol types described above (remote
802 marine, regional marine and black carbon (BC)) were carried out. Due to the low number of days with
dust classification (3 days), this aerosol type is not included. For the surface in-situ measurements, the
804 categories in Cappa's matrix are used for aerosol classification as described above. For the rest of the
806 atmospheric column, the grouping of aerosol types is based on Toledano et al. (2007b), which uses the
relationship between AOD at 440 nm and extinction Ångström exponent at 440 nm/870 nm to identify
808 aerosol type. Table 3 shows the criterion used. To select cases with the representative aerosol type,
data were only considered when the aerosol category for the surface in-situ measurements matched the
810 aerosol category of the column measurements (i.e., Table 3). When the aerosol types match for in-situ
812 and column measurements it is assumed that the mixing layers are well mixed and a homogeneous
vertical aerosol profile is present in the troposphere and boundary layers. In order to know that the
aerosol optical properties of these subsets are the same as those in Figure 5, an statistical analysis has
been carried out and it is shown in Figure 3S.

814 The frequency histogram of DRE_{TOA} (Figure 6b) and statistical parameters (Figure 6c) of each aerosol
816 type (remote marine and BC) and a mixture of both particle types (regional marine), are shown. In the

case of remote marine aerosol, all DRE_{TOA} values are below -4 W m^{-2} bin, with maxima at -2 W m^{-2} bin. For the anthropogenic aerosol type (labeled BC), DRE_{TOA} ranges from -5.0 W m^{-2} to -13.0 W m^{-2} , with maximum at -6.0 W m^{-2} . The frequency distribution for DRE_{TOA} of regional marine aerosol falls between that of the remote marine and BC aerosol, as it consists of a mixture of sea salt and anthropogenic aerosol.

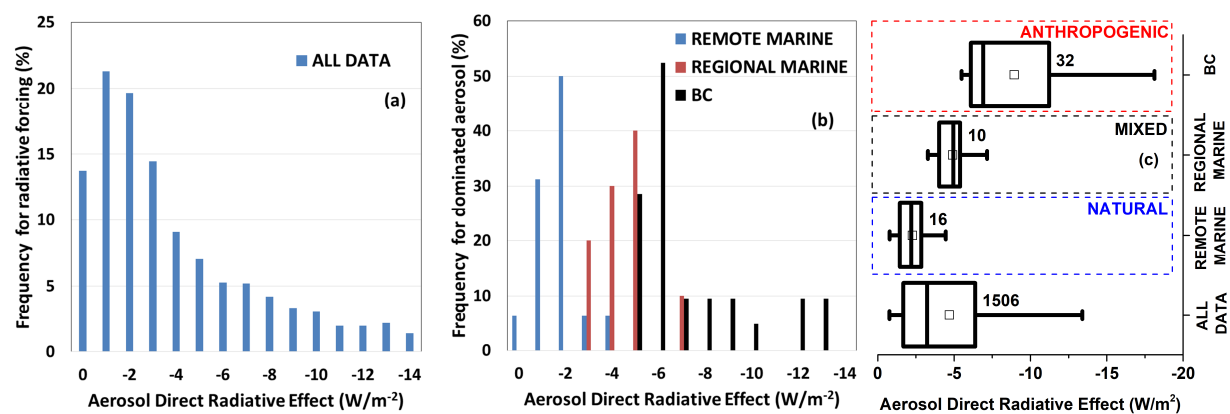


Figure 6. Frequency histogram for the aerosol direct radiative effect at the top of the atmosphere (DRE_{TOA}) at ARN, (a) for all data and (b) for remote marine, regional marine and black carbon (BC-dominated) aerosol types. (c) Statistical analysis by hourly means of DRE_{TOA} . Vertical line is the median (50th percentile), edges of box are 25th and 75th percentiles, whiskers are 5th and 95th percentiles. Square is the mean value. Number of data used in each aerosol type is shown near each box.

Aerosol Typing	At surface level <i>Cappa et al. (2016)</i>		Integrated column <i>Toledano et al. (2007b)</i>	
	AAE	SAE	AOD	EAE
Remote marine	0-1	<1	<0.10	0.0-1.5
Regional marine	0-1	1-3	0.10-0.20	1.0-1.5
BC	1-1.5	1-3	0.20-0.35	>1.05

Table 3. Criterion for selecting aerosol types as remote marine, regional marine and black carbon (BC) at surface level (left) and total aerosol column (right). AOD and extinction Ångström exponent (EAE) for BC dominated aerosol type are referred to as continental in Toledano et al. (2007b).

Figure 6 suggests that natural and anthropogenic aerosols at ARN lead to a cooling of the climate system through the direct aerosol effect at medium latitudes, and this cooling effect is higher for aerosol types related to anthropogenic activities, primarily due to the higher loading of these aerosols. Since the industrial revolution, human activities have increased the concentrations of components in the atmosphere, impacting the radiative balance of the Earth system. The IPCC Fifth Assessment Report (IPCC, 2014) shows that the anthropogenic radiative forcing is positive, therefore the direct radiative effect has shifted to higher values from pre-industrial to present-day but the overall aerosol radiative effect continues to be cooling. The results found in our work may be useful to modelers in order to compare with estimated radiative effect of aerosols at present-day and may add in the determination of radiative forcing trends both for the natural and anthropogenic aerosols (e.g. Schulz et al., 2006; Skeie et al., 2011).

4. MAIN CONCLUSIONS

Analyses of near-surface, in-situ, spectral aerosol light scattering (11 years) and absorption (4 years) measurements on the southwestern coast of Spain are reported in this study to develop understanding of: (1) the typical values, temporal variability and trends of aerosol optical properties, (2) the types of aerosol observed based on proxies of the aerosol size and composition and (3) the radiative effect as a function of aerosol type. The sampling site, at El Arenosillo (ARN) observatory in the southwest of the Iberian Peninsula, is representative of other Atlantic coastal environments in southwestern Europe.

854 A trend analysis on aerosol scattering coefficient (2006-2016 period) for the sub-10 size fraction
856 indicates statistically significant decreasing trends for March, May-June and September-October
858 periods, with a trend values ranging from -1.5 to -2.8 $Mm^{-1}/year$. For the (2009-2016) period, the
860 decreasing trend is less obvious and is only statistically significant for June and September months. For
862 scattering Ångström exponent there were two months with statistically significant trends (June and
864 October): an increasing trend during June with a rate of 0.059/year and a decreasing trend during
866 October with a rate of -0.060/year. The trends observed may be a combination of one or more of the
868 following causes: (1) reduction of Saharan desert dust air masses arriving in the south of Spain, (2) a
870 decrease in particle loading in desert dust air masses and (3) a drop in particle loading in anthropogenic
872 influenced air masses.

874 Aerosol particles in the different size cuts exhibit different characteristics. Scattering particles are found
876 within both size fractions, while absorbing particles are mainly within the sub1-micron size range. The
878 relationship between scattering and absorption Ångström exponents provides information on aerosol
880 composition and size, and suggests several primary aerosol types. The sub1-micron size cut comprises
882 black carbon dominated, mixed black and brown carbon and sea spray with anthropogenic influences
884 (regional marine) aerosol types. The main sources of super-micrometer particles appear to be a pure sea
886 spray aerosol or combination of desert dust and sea spray.

888 The aerosol properties have been segregated by the aerosol type and the aerosol optical property
889 statistics have been determined. Dust particles exhibit the highest scattering coefficient demonstrating
890 the intensity of occasional dust events. The absorption coefficient is highest for brown and black carbon
891 mix, while the lowest absorption values are observed for regional marine aerosol. Aerosol direct
892 radiative effect at the top of the atmosphere (DRE_{TOA}) was calculated based on measurements for
893 several aerosol types. The hourly mean value obtained for DRE_{TOA} regardless of type was $-4.7 W m^{-2}$ with
894 standard deviation, $\pm 4.2 W m^{-2}$ and 5th and 95th percentiles of $-13.4 W m^{-2}$ and $-0.77 W m^{-2}$, respectively.
895 For remote marine aerosol the frequency histogram of DRE_{TOA} showed all DRE_{TOA} values to be below $-4 W m^{-2}$, with the maximum at $-2 W m^{-2}$. For the anthropogenic aerosol type (labeled BC aerosol), DRE_{TOA}
896 ranges from $-5 W m^{-2}$ to $-13 W m^{-2}$, with maximum at $-6 W m^{-2}$. The frequency distribution for DRE_{TOA} of
897 regional marine aerosol (a mix of sea salt and anthropogenic aerosol) ranges from $-3 W m^{-2}$ to $-7 W m^{-2}$.
898 The variability observed in DRE_{TOA} is mainly dependent on the variability in AOD, as the backscatter
899 fraction and the single scattering albedo tend to counteract each other in the radiative forcing efficiency
900 equation.

902 This analysis demonstrates that aerosol optical properties can be used to identify the aerosol types, and
903 thus to distinguish particle sources and to indicate the importance of each source to the atmospheric
904 radiative effect. This typing and the associated aerosol characteristics may also be used to understand
905 uncertainties in remote sensing retrieval products and to correctly parameterize aerosol properties in
906 model evaluation studies, in order to properly simulate the forcing by aerosols.

908 5. DATA AVAILABILITY

909 The nephelometer and CLAP measurements at El Arenosillo are included in the NOAA/ESRL Federated
910 Aerosol Network (www.esrl.noaa.gov/gmd/aero/net/arn/index.html; Andrews et al., 2018). Raw data
911 are submitted in Near-Real-Time system to World Data Center for Aerosols (WDCA) and edited and
912 hourly data are submitted annually and can be retrieved from the EBAS data bank (<http://ebas.nilu.no/>).

914 Acknowledgments

916 This work was partially supported by the Spanish Ministry of Science and Technology (MINECO) through
917 the AVATAR project (CGL2014-55230-R) and the European Union's Horizon 2020 research and
918 innovation programme under grant agreement N° 654109 (ACTRIS-2). The authors would like to express
919 their gratitude to the NOAA Air Resources Laboratory for the HYSPLIT model. This paper would not be
920 possible without the support of several technicians who help to maintain the instruments as M. Boa, J.A.

906 Díaz and S. König or the software as D. Hageman, as well as the interest of scientific staff as B.A. de la
Morena, M. Gil, M.J. Gutierrez and A.L. Moratilla.

908

References

910 Anderson, T.L., Covert, D.S., Marshall, S.F., Laucks, M.L., Charlson, R.J., Waggoner, A.P., Ogren, J.A.,
Caldow, R., Holm, R.L., Quant, F.R., Sem, G.J., Wiedensohler, A., Ahlquist, N.A., and Bates, T.S.
912 1996. Performance characteristics of a high-sensitivity, three wavelength, total
scatter/backscatter nephelometer. *Am. Meteorol. Soc.*, 13, 967-986.

914 Anderson, T. L. and Ogren, J. A. 1998. Determining Aerosol Radiative Properties Using the TSI 3563
Integrating Nephelometer, *Aerosol Sci. Technol.*, 29, 57-69, doi:10.1080/02786829808965551.,

916 Andrews, E., Sheridan, P.J., Fiebig, M., McComiskey, A., Ogren, J.A., Arnott, P., Covert, D., Elleman, R.,
Gasparini, R., Collins, D., Jonsson, H., Schmid, B., Wang, J. 2006. Comparison of methods for
918 deriving aerosol asymmetry factor. *J. Geophys. Res.*, 111, D05S04, doi:10.1029/2004JD005734.

920 Andrews, E., Ogren, J.A., Bonasoni, P., Marinoni, A., Cuevas, E. et al., 2011. Climatology of aerosol
radiative properties in the free troposphere. *Atmos. Res.*, 102, 365-393.

922 Andrews, E., Sheridan, P.J., Ogren, J.A., Hageman, D., Jefferson, A., Wendell, J., Alstuey, A., Alados-
Arboledas, L., Bergin, M., Ealo, M., Gannet Hallar, A., Hoffer, A., Kalapov, I., Keywood, M., Kim, J.,
924 Kim, S.-W., Kolonjari, F., Labuschagne, C., Lin, N.-H., Macdonald, A.M., Mayol-Bracero, O.,
McCubbin, I.B., Pandolfi, M., Reisen, F., Sharma, S., Sherman, J.P., Sorribas, M., Sun, J. 2017.
Overview of the NOAA/ESRL Federated Aerosol Network. *Bull. Amer. Meteor. Soc.*, In press.

926 Bond, T.C., Anderson, T.L. and Campbell, D. 1999. Calibration and intercomparison of filter-based
measurements of visible light absorption by aerosols. *Aerosol Sci. Technol.*, 30, 582-600.

928 Boucher, O., Randall, D., Artaxo, P., Bretherton, C., Feingold, G., Forster, P., Kerminen, V. M., Kondo, Y.,
Liao, H., Lohmann, U., Rasch, P., Satheesh, S. K., Sherwood, S., Stevens, B., and Zhang, X. Y.: Clouds
930 and aerosols, in: *Climate Change 2013: The Physical Science Basis, Contribution of Working Group*
I to the Fifth Assessment Report of the Intergovernmental Panel on Climate Change, edited by:
932 Stocker, T. F., Qin, D., Plattner, G.-K., Tignor, M., Allen, S. K., Boschung, J., Nauels, A., Xia, Y., Bex,
V., and Midgley, P. M., 571-657, Cambridge University Press, Cambridge, United Kingdom and
934 New York, NY, USA, 2013.

936 Cachorro, V.E., Burgos, M.A., Mateos, D., Toledano, C., Bennouna, Y., Torres, B., De Frutos, A.M.,
Heguedas, A. 2016. Inventory of African desert dust events in the north-central Iberian Peninsula
in 2003-2014 based on sun-photometer-AERONET and particulate-mass-EMEP data. *Atmos.*
938 *Chem. Phys.*, 16, 8227-8248, <http://dx.doi.org/10.5194/acp-16-8227-2016>.

940 Cappa, C.D., Kolesar, K.R., Zhang, X., Atkinson, D.B., Pekour, M.S., Zaveri, R.A., Zelenyuk, A., Zhang, Q.
2016. Understanding the optical properties of ambient sub- and supermicron particulate matter:
results from the CARES 2010 field study in northern California. *Atmos. Chem. Phys.*, 16, 6511-
942 6535.

944 Carrico, C.M., Rood, M.J., and Ogren, J.A. 1998. Aerosol light scattering properties at Cape Grim,
Tasmania, during the First Aerosol Characterization Experiment (ACE1). *J. Geophys. Res.*, 103, NO,
D13; 16565-16574.

946 Cazorla, A., Bahadur, R., Suski, K.J., Cahill, J.F., Chand, D., Schmid, B., Ramanathan, V., Prather, K.A.,
2013. Relating aerosol absorption due to soot, organic carbon, and dust to emission sources
948 determined from in-situ chemical measurements. *Atmos. Chem. Phys.* 13, 9337-9359.

950 Collaud Coen, M., Weingartner, E., Nyeki, S., Cozic, J., Henning, S., Verheggen, B., Gehrig, R., and
Baltensperger, U. 2007. Long-term trend analysis of aerosol variables at the high-alpine site
Jungfraujoch. *J. Geophys. Res.* 112, D13213, doi:10.1029/2006JD007995.

952 Córdoba-Jabonero, C., Sorribas, M., Guerrero-Rascado, J.L., Adame, J.A., Hernández, Y., et al., 2011.
Synergetic monitoring of Saharan dust plumes and potential impact on surface: a case study of
954 dust transport from Canary Islands to Iberian Peninsula. *Atmos. Chem. Phys.* 11, 3067-3091.

956 Costabile, F., Barnaba, F., Angelini, F., Gobbi, G.P., 2013. Identification of key aerosol populations
through their size and composition resolved spectral scattering and absorption. *Atmos. Chem.
Phys.* 13, 2455-2470.

958 Cuevas, E., Camino, C., Benedetti, A., Basart, S., Terradellas, E., Baldasano, J.M., Morcrette, J.J.,
 960 Marticorena, B., Goloub, P., Mortier, A., Berjón, A., Hernández, Y., Gil-Ojeda, M., and Schulz, M.
 962 2015. The MACC-II 2007-2008 reanalysis: atmospheric dust evaluation and characterization over
 964 northern Africa and the Middle East. *Atmos. Chem. Phys.*, 15, 3991-4024.

966 Doherty, S.J., Quinn, P.K., Jefferson, A., Carrico, C.M., Anderson, T.L. and Hegg, D. 2005. A comparison
 968 and summary of aerosol optical properties as observed in situ from aircraft, ship, and land during
 970 ACE-Asia. *J. Geophys. Res.*, 110, D04201, doi:10.1029/2004JD004964.

972 Eck, T.F., Holben, B.N., Reid, J.S., Xian, P., Giles, D.M., Sinyuk, A., Smirnov, A., Schafer, J.S., Slutsker, I.,
 974 Kim, J., Koo, J.-H., Choi, M., Kim, K.C., Sano, I., Arola, A., Sayer, A.M., Levy, R.C., Munchak, L.A.,
 976 O'Neill, N.T., Lyapustin, A., Hsu, N.C., Randles, C., Da Silva, A.M., Buchard, V., Govindaraju, R.C.,
 978 Hyer, E., Crawford, J.H., Wang, P., and Xia, X. 2018. Observations of the interaction and transport
 980 of fine mode aerosols with cloud and/or fog in Northeast Asia from Aerosol Robotic Network and
 982 satellite remote sensing. *J. Geophys. Res.*, 123, 10, 5560-5587, doi:10.1029/2018JD028313.

984 Estellés, V., Campanelli, M., Smyth, T.J., Utrillas, M.P., Martínez-Lozano, J.A. 2012. Evaluation of the new
 986 ESR network software for the retrieval of direct sun products from CIMEL CE318 and PREDE
 988 POM01 sun-sky radiometers. *Atmos. Chem. Phys.* 12, 11619-11360.

990 Fiebig, M., and Ogren, J.A., 2006. Retrieval and climatology of the aerosol asymmetry parameter in the
 992 NOAA aerosol monitoring network. *J. Geophys. Res.*, 111, D21204, doi:10.1029/2005JD006545.

994 Fierz-Schmidhauser, R., Zieger, P., Vaishya, A., Monahan, C., Bialek, J. and co-authors. 2010b. Light
 996 scattering enhancement factors in the marine boundary layer (Mace Head, Ireland). *J. Geophys.
 998 Res.*, 115, D20204. DOI: 10.1029/2009JD013755.

1000 Gilbert, R.O. 1987. *Statistical Methods for Environmental Pollution Monitoring*. United States. ISBN: 0-
 1002 442-23050-8. <https://www.osti.gov/servlets/purl/7037501>.

1004 Heald, C.L., Ridley, D.A., Kroll, J.H., Barrett, S.R.H., Cady-Pereira, K.E., Alvarado, M. J. and Holmes, C.D.
 1006 2014. Contrasting the direct radiative effect and direct radiative forcing of aerosols. *Atmos. Chem.
 1008 Phys.*, 14, 5513-5527, doi:10.5194/acp-14-5513-2014.

1010 Holben, B.N., Eck, T.F., Holben, B.N., Slutsker, I., Buis, J.P., Setzer, A., Vermote, E., Reagan, J.A., Kaufman,
 1012 Y., Nakajima, T., Lavenu, F., Smirnov, A. 1998. AERONET a federated instrument network and data
 1014 archive for aerosol characterization. *Remote Sens. Environ.* 66, 1-16.

1016 Horvath, H., Kasahara, M., Tohno, S., Olmo, F.J., Lyamani, H., Alados-Arboledas, L., Quirantes, A.,
 1018 Cachorro, V. Relationship between fraction of backscattered light and asymmetry parameter.
 1020 *Journal of Aerosol Science*, <http://dx.doi.org/10.1016/j.jaerosci.2015.09.003>.

1022 IPCC. 2014. *Climate Change 2013: The Physical Science Basis. Contribution of Working Group I to the
 1024 Fifth Assessment Report of the IPCC*. Cambridge University Press: Cambridge, UK.

1026 Kahn, R.A., Berkoff, T.A., Brock, C., Chen, G., Ferrere, R.A., Ghan, S., Hansico, T.F., Hegg, D.A., Martins,
 1028 J.V., McNaughton, C.S., Murphy, D.M., Ogren, J.A., Penner, J.E., Pilewskie, P., Seinfeld, J.H., and
 1030 Worsnop, D.R. 2017. SAM-CAAM: a concept for acquiring systematic aircraft measurements to
 1032 characterize aerosol air masses. *Bull. Amer. Meteor. Soc.*, Vol. 98, No. 10, doi:10.1175/BAMS-D-
 1034 16-0003.1

1036 Li, J., Carlson, B.E., Dubovick, O., and Lacis, A.A. 2014. Recent trends in aerosol optical properties derived
 1038 from AERONET measurements. *Atmos. Chem. Phys.*, 14, 12271-12289,
 1040 <http://dx.doi.org/10.5194/acp-14-12271-2014>.

1042 Lyamani, H., Olmo, F. J. and Alados-Arboledas, L. 2010. Physical and optical properties of aerosols over
 1044 an urban location in Spain: seasonal and diurnal variability. *Atmos. Chem. Phys.* 10, 239-254.

1046 Mao, K.B., Ma, Y., Xia, L., Chen, W.Y., Shen, X.Y., He, T.J., and Xu, T.R. 2014. Global aerosol change in the
 1048 last decade: and analysis based on MODIS data. *Atmos. Environ.*, 94, 680-686.

1050 Markowicz, K.M., Flatau, P.J., Quinn, P.K., Carrico, C.M., Flatau, M.K., Vogelmann, A.M., Bates, D., Liu,
 1052 M., Rood, M.J. 2003. Influence of relative humidity on aerosol radiative forcing: and ACE-Asia
 1054 experiment perspective. *J. Geophys. Res.*, 108, D23, 8662, doi:10.1029/2002JD003066.

1056 Mateos, D., Antón, M., Toledano, C., Cachorro, V.E., Alados-Arboledas, L., Sorribas, M., Costa, M.J., and
 1058 Baldasano, J.M. 2014. Aerosol radiative effects in the ultraviolet, visible, and near-infrared

1010 spectral ranges using long-term aerosol data series over the Iberian Peninsula. *Atmos. Chem. Phys.*, 14, 13497-13514, <https://doi.org/10.5194/acp-14-13497-2014>.

1012 Moosmüller, H., and Ogren, J.A. 2017. Parameterization of the aerosol upscatter fraction as function of the backscatter fraction and their relationships to the asymmetry parameter for radiative transfer calculations. *Atmosphere*, 8, 133, doi:10.3390/atmos8080133.

1014 Ogren, J.A. 2010. Comment on “Calibration and intercomparison of filter-based measurements of visible light absorption by aerosols”. *Aerosol Sci. and Technol.*, 44, 589-591.

1016 Ogren, J.A. Wendell, J., Andrews, E., and Sheridan, P.J. 2017. Continuous light absorption photometer for long.-term studies. *Atmos. Meas. Tech.*, 10, 4805-4818.

1018 Oke, T.R. 1987. Boundary layer climates, Second Edition, Methuen, London.

1020 Pandolfi, M., Alados-Arboledas, A., Alastuey, A., Andrade, M., Artiñano, B., Backman, J., et al. 2017. A European aerosol phenomenology-6: scattering properties of atmospheric aerosol particles from 28 ACTRIS sites. *Atmos. Chem. Phys.*, 18, 7877-7911, <https://doi.org/10.5194/acp-18-7877-2018>.

1022 Péré, J.-C., Rivellini, L., Crumeyrolle, S., Chiapello, I., Minvielle, F., Thieuleux, F., Choel, M., Popovici, I. 2024 Simulation of African dust properties and radiative effects during the 2015 SHADOW campaign in Senegal. *Atmos. Res.*, 199, 14-28, <https://doi.org/10.1016/j.atmosres.2017.07.027>.

1026 Pereira, S. N., Wagner, F. and Silva, A. M. 2011. Seven years of measurements of aerosol scattering properties, near the surface, in the southwestern Iberia Peninsula. *Atmos. Chem. Phys.* 11, 17-29.

1028 Roberts, G., Wooster, M.J., and Lagoudakis, E. 2009. Annual and diurnal African biomass burning temporal dynamics. *Biogeosciences*, 6, 849-866.

1030 Rodríguez, S., Alastuey, A., Alonso-Pérez, S., Querol, X., Cuevas, E., Abreu-Afonso, J., Viana, M., Pérez, N., Pandolfi, M., and De la Rosa, J. 2011. Transport of desert dust mixed with North African industrial pollutants in the subtropical Saharan Air Layer. *Atmos. Chem. Phys.*, 11, 6663-6685, <https://doi.org/10.5194/acp-11-6663-2011>.

1032 Schmeisser, L., Andrews, E., Ogren, J.A., Sheridan, P., Jefferson, A., Sharma, S., Kim, J.E., Sherman, J.P., Sorribas, M., Kalapov, I., Arsov, T., Angelov, C., Mayol-Bracero, O.L., Labuschagne, C., Kim, S.-W., Hoffer, A., Lin, N.-H., Chia, H.-P., Bergin, M., Sun, J., Liu, P., Wu, H. 2017. Classifying aerosol type using in situ surface spectral aerosol optical properties. *Atmos. Chem. Phys.*, 17, 12097-12120.

1034 Schulz, M., Textor, C., Kinne, S., Balkanski, Y., Bauser, S., Berntsen, T., Barglen, T., Boucher, O., Dentener, F., Guibert, S., Isaksen, I.S.A., Iversen, T., Koch, D., Kirkevåg, A., Liu, X., Montanaro, V., Myhre, G., Penner, J.E., Pitari, G., Reddy, S., Seland, Ø, Stier, P., Takemura, T. 2006. Radiative forcing by aerosols as derived from the AeroCom present-day and pre-industrial simulations. *Atmos. Chem. Phys.*, 6, 5225-5246.

1036 Seinfeld, J. H. and Pandis, S. N. 1998. Atmospheric chemistry and physics: from air pollution to climate change, Wiley, New York, 100–103.

1040 Sheridan, P.J. and Ogren, J.A. 1999. Observation of the vertical and regional variability of aerosol optical properties over central and eastern North America. *J. Geophys. Res.*, 104 (D14), 16793-16805.

1042 Sheridan, P.J., Jefferson, A., Ogren, J.A. 2002. Spatial variability of submicrometer aerosol radiative properties over the Indian Ocean during INDOEX. *J. Geophys. Res.*, 107, D19, 8011, 10.1029/2000JD000166.

1044 Sheridan, P., Andrews, E., Schmeisser, L., Vasel, B., and Ogren, J. 2016. Aerosol Measurements at South Pole: Climatology and Impact of Local Contamination. *Aerosol Air Qual. Res.*, 16, 855–872.

1046 Sheridan, P. J., Sheridan, P. J., Ogren, J. A., Andrews, E., Hageman, D., Schmeisser, L., Jefferson, A., and Sharma, S. 2015. A multi-year study of lower tropospheric aerosol variability and systematic relationships from four North American regions, *Atmos. Chem. Phys.*, 15, 12487–12517, <https://doi.org/10.5194/acp-15-12487-2015>.

1048 Skeie, R.B., Berntsen, T., Myhre, G., Pedersen, C.A., Ström, J., Gerland, S., and Ogren, J.A. 2011. Black carbon in the atmosphere and snow, from pre-industrial times until present. *Atmos. Chem. Phys.*, 11, 6809-6836.

1050 Sorribas, M., De la Morena, B. A., Wehner, B., López, J. F., Prats, N. and co-authors. 2011. On the sub-micron aerosol size distribution in a coastal-rural site at El Arenosillo Station (SW-Spain). *Atmos. Chem. Phys.* 11, 11185_11206.

1052

1054

1056

1058

1060

1062 Sorribas, M., Ogren, J.A., Olmo, F.J., Quirantes, A., Fraile, R., Gil-Ojeda, M., and Alados-Arboledas, L.
1064 2015a. Assessment of African desert dust episodes over the southwest Spain at sea level using in situ aerosol optical and microphysical properties. *Tellus B*, 67, 27482, <http://dx.doi.org/10.3402/tellusb.v67.27482>.

1066 Sorribas, M., Olmo, F.J., Quirantes, A., Lyamani, H., Gil-Ojeda, M., Alados-Arboledas, L., and Horvath, H.
1068 2015b. Role of spheroidal particles in closure studies for aerosol microphysical-optical properties. *Q.J.R. Meteorol. Soc.*, doi:10.1002/qj.2557.

1070 Sorribas, M. Adame, J. A. Olmo, F. J. Vilaplana, J.M., Gil-Ojeda, M., Alados-Arboledas, L. 2015c. A long-term study of new particle formation in a coastal environment: Meteorology, gas phase and solar radiation implications. *Sci. Total Environ.*, 511, 723-737, DOI: 10.1016/j.scitotenv.2014.12.011.

1072 Sorribas, M., Adame, J.A., Andrews, E., Yela, M. An anomalous African dust events and its impact on aerosol radiative forcing on the Southwest Atlantic coast of Europe in February 2016. 2017. *Sci. Total Environ.*, <https://doi.org/10.1016/j.scitotenv.2017.01.064>

1074 Takamura, T., Nakajima, T., 2004. Overview of SKYNET and its activities. *Pure Appl. Opt.* 7, 3303-3303.

1076 Toledano, C., Cachorro, V.E., de Frutos, A.M., Sorribas, M., Prats, N., and de la Morena, B.A. 2007a. Inventory of African desert dust events over the southwestern Iberian Peninsula in 2000-2005 with an AERONET Cimel Sun Photometer. *J. Geophys. Res.*, <http://dx.doi.org/10.1029/2006JD008307>.

1080 Toledano, C., Cachorro, V.E., Berjón, A., De Frutos, A.M., Sorribas, M., De la Morena, B.A., Goloub, P., 2007b. Aerosol optical depth and Ångström exponent climatology at El Arenosillo AERONET site (Huelva, Spain). *Q. J. R. Meteorol. Soc.* 133 (624), 795–807.

1082 Toledano, C., Cachorro, V. E., De Frutos, A. M., Torres, B., Berjón, A., Sorribas, M., and Stone, R. S. 2009. Airmass classification and analysis of aerosol types at El Arenosillo (Spain), *J. Appl. Meteorol. Clim.*, 48, 962–981, 2009.

1084 Titos, G., Lyamani, H., Cazorla, A., Sorribas, M., Foyo-Moreno, I., Wiedensohler, A., and Alados-Arboledas, L. 2014a. Study of the relative humidity dependence of aerosol Light-scattering in southern Spain. *Tellus B*, 66, 24536, <http://dx.doi.org/10.3402/tellusb.v66.24536>.

1088 Titos, G., Jefferson, A., Sheridan, P. J., Andrews, E., Lyamani, H., Alados-Arboledas, L., and Ogren, J.A. 2014b. Aerosol light-scattering enhancement due to water uptake during TCAP campaign. *Atmos. Chem. Phys.* 14, 7031-7043, doi:10.5194/acp-14-7031-2014.

1092 Willeke, K. and Baron, P. A.: *Aerosol measurements principles, techniques and applications*, Van Nostrand Reinhold, New York, USA, 143–195, 1993.

1094 WMO, 2016. WMO//GAW aerosol measurement procedures, guidelines and recommendations. 2nd edition. GAW Report no. 227.

1096 Zanatta, M., Gysel, M., Bukowiecki, N., Müller, T., Weingartner, E., Areskoug, H., Fiebig, M., Yttri, K.E., Mihalopoulos, N., Kouvarakis, G., Beddows, D., Harrison, R.M., Cavalli, F., Putaud, J.P., Spindler, G., Wiedensohler, A., Alastuey, A., Pandolfi, M., Sellegri, K., Swietlicki, E., Jaffrezo, J.L., Baltensperger, U., and Laj, P. 2016. A European aerosol phenomenology-5: climatology of black carbon optical properties at 9 regional background sites across Europe. *Atmos. Environ.*, 145, 346-364, <http://dx.doi.org/10.1016/j.atmosenv.2016.09.035>.

1100 Zhang, J., and Reid, J.S. 2009. An analysis of clear sky and contextual biases using an operational over ocean MODIS aerosol product. *Geophys. Res. Lett.*, 36, L15824, doi:10.1029/2009GL038723.

1102 Zieger, P., Fierz-Schmidhauser, R., Weingartner, E., and Baltensperger, U. 2013. Effects of relative humidity on aerosol light scattering: results from different European sites. *Atmos. Chem. Phys.*, 13, 10609-10631.

1106